

AD-A162 119

OPTIMIZATION OF TIP STORE MODELING(U) OKLAHOMA UNIV  
NORMAN SCHOOL OF AEROSPACE MECHANICAL AND NUCLEAR  
ENGINEERING A G STRIZ ET AL MAR 85 AFOSR-TR-85-1089

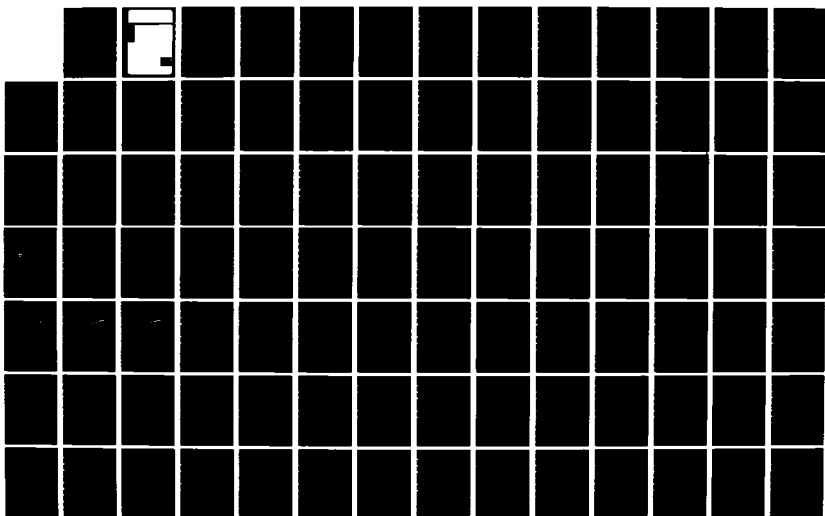
1/2

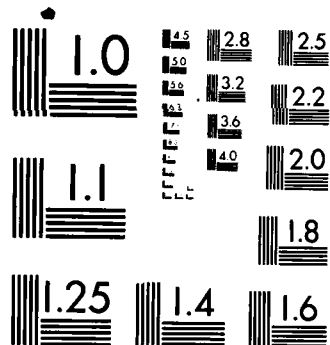
UNCLASSIFIED

AFOSR-83-0184

F/G 28/4

NL





MICROCOPY RESOLUTION TEST CHART  
NATIONAL BUREAU OF STANDARDS-1963-A

am  
he

AD-A162 119

DTIC FILE COPY

DTIC  
ELECTE  
DEC 6 1985  
S  
A

# REPORT DOCUMENTATION PAGE

1a. REPORT SECURITY CLASSIFICATION <b>Unclassified</b>		1b. RESTRICTIVE MARKINGS	
2a. SECURITY CLASSIFICATION AUTHORITY		3. DISTRIBUTION/AVAILABILITY STATEMENT  <b>Approved for public release, distribution unlimited</b>	
2b. DECLASSIFICATION/DOWNGRADING SCHEDULE			
4. PERFORMING ORGANIZATION REPORT NUMBER(S)		5. MONITORING ORGANIZATION REPORT NUMBER(S)  <b>AFOSR-TR- 85-1089</b>	
6a. NAME OF PERFORMING ORGANIZATION  <b>UNIVERSITY OF OKLAHOMA</b>	6b. OFFICE SYMBOL (If applicable)	7a. NAME OF MONITORING ORGANIZATION  <b>AFOSR/NA</b>	
6c. ADDRESS (City, State and ZIP Code) <b>SCHOOL OF AEROSPACE, MECHANICAL &amp; NUCLEAR ENGR NORMAN, OKLAHOMA 73019</b>		7b. ADDRESS (City, State and ZIP Code)  <b>BOLLING AFB DC 20332-6448</b>	
8a. NAME OF FUNDING/SPONSORING ORGANIZATION <b>AIR FORCE OFFICE OF SCIENTIFIC RESEARCH</b>	8b. OFFICE SYMBOL (If applicable) <b>AFOSR/NA</b>	9. PROCUREMENT INSTRUMENT IDENTIFICATION NUMBER  <b>AFOSR-83-0184</b>	
8c. ADDRESS (City, State and ZIP Code)  <b>BOLLING AFB, DC 20332-6448</b>		10. SOURCE OF FUNDING NOS.	
11. TITLE (Include Security Classification) <b>OPTIMIZATION OF TIP STORE MODELING (UNCLASSIFIED)</b>		PROGRAM ELEMENT NO. <b>61102F</b>	PROJECT NO. <b>2307</b>
12. PERSONAL AUTHOR(S) <b>ALFRED G STRIZ, SUNG-KUK JANG</b>		TASK NO. <b>A4</b>	WORK UNIT NO.
13a. TYPE OF REPORT <b>FINAL</b>	13b. TIME COVERED <b>FROM MAY 83 TO SEP 84</b>	14. DATE OF REPORT (Yr., Mo., Day) <b>1985 March</b>	
15. PAGE COUNT <b>103</b>		16. SUPPLEMENTARY NOTATION	
17. COSATI CODES		18. SUBJECT TERMS (Continue on reverse if necessary and identify by block number)	
FIELD	GROUP	SUB. GR.	
		TIP STORE ,WING, MODELING, UNSTEADY AFRODYNAMICS	
19. ABSTRACT (Continue on reverse if necessary and identify by block number)			
<p>Due to the high cost of performing detailed three-dimensional flutter analyses for aircraft which are carrying large numbers and types of external stores, it is often not economically feasible to include sophisticated store aerodynamics especially when they will not cause significant changes to the flutter results. Thus, the stores are presently often modeled as simple flat plates. This tends to decrease the accuracy of the computed pressure distributions as the spanwise flow field and the wing-body interaction are not represented correctly.</p> <p>In this report, therefore, two methods, a doublet lattice method for subsonic flow (computer code H7WC by Giesing, Kalman, and Rodden) and a kernel function method for subsonic and supersonic flow (computer code ANKF by Cunningham) are used for the computation of unsteady pressure distributions and forces on an F-5 wing with a tip mounted launcher/store combination for various store models consisting of simple flat plates, endplated, and axisymmetric bodies. The resulting aerodynamic data are compared to existing experimental</p>			
20. DISTRIBUTION/AVAILABILITY OF ABSTRACT  UNCLASSIFIED/UNLIMITED <input checked="" type="checkbox"/> SAME AS RPT. <input type="checkbox"/> DTIC USERS <input type="checkbox"/>		21. ABSTRACT SECURITY CLASSIFICATION  <b>Unclassified</b>	
22a. NAME OF RESPONSIBLE INDIVIDUAL  <b>JAMES D WILSON</b>		22b. TELEPHONE NUMBER (Include Area Code) <b>767-4935</b>	22c. OFFICE SYMBOL  <b>AFOSR/NA</b>

and numerical results for the same wing/store combination.

The store modeling was optimized for simplicity and accuracy with respect to the aerodynamic forces and pressures. The wing-body interaction was improved without a considerable increase in complexity, i.e. panel number, and thus computational effort.

*wing body configuration; aerodynamic stability*

OPTIMIZATION OF TIP STORE MODELING

Alfred G. Striz and Sung-Kuk Jang  
University of Oklahoma  
Norman, OK 73019

March 1985

Chief, 1.

Technical Report  
Final Report for Period May 1983 - September 1984

Approved for public release; distribution unlimited.

Air Force Office of Scientific Research  
Air Force Systems Command  
Bolling Air Force Base, D.C. 20332



## FOREWORD

This report was prepared by Dr. Alfred G. Striz of the School of Aerospace, Mechanical and Nuclear Engineering at the University of Oklahoma in Norman, OK, under AFOSR Grant 83-0184, "Optimization of Tip Store Modeling". The research was administered by Captain Dwight R. McGhee and the program manager was Dr. James D. Wilson, both of the Air Force Office of Scientific Research at Bolling Air Force Base, D.C.

The report covers work conducted during the grant period from May 1983 to September 1984. Dr. Alfred G. Striz was the principal investigator, Sung-Kuk Jang was the graduate research assistant. Bob Bunton and Dave Belk of the Air Force Armament Laboratory at Eglin Air Force Base, FL, and Herbert Cunningham of the NASA-Langley Research Center in Hampton, VA, were helpful in providing needed information.

Sung-Kuk Jang will receive his M.S. degree for this research in March of 1985 with a thesis entitled "Optimization of Wing Tip Store Modeling for Aircraft in Subsonic and Supersonic Flow". He presented partial results of this work previously at the 1984 meeting of the Oklahoma Academy of Sciences in Ada, OK,

and at the 1985 AIAA/ASME Symposium VII in Norman, OK.

A paper with the title "Optimization of Tip Store Modeling" by Dr. Alfred G. Striz and Sung-Kuk Jang will be submitted to AIAA for possible publication in the Journal of Aircraft.



## TABLE OF CONTENTS

FOREWORD . . . . .	iii
TABLE OF CONTENTS . . . . .	v
LIST OF SYMBOLS . . . . .	vi
LIST OF FIGURES . . . . .	viii
LIST OF TABLES . . . . .	x

<u>Chapter</u>	<u>page</u>
I. INTRODUCTION . . . . .	1
Background . . . . .	2
Scope of Present Research . . . . .	4
II. DEVELOPMENT OF THEORY . . . . .	7
Doublet Lattice Method . . . . .	9
Introduction . . . . .	9
Theoretical Development . . . . .	12
Kernel Function Method . . . . .	17
Introduction . . . . .	17
Theoretical Development . . . . .	18
III. NUMERICAL MODELING . . . . .	24
Doublet Lattice Method . . . . .	29
Kernel Function Method . . . . .	29
IV. RESULTS . . . . .	35
Clean Wing Case . . . . .	36
Doublet Lattice Method . . . . .	39
Kernel Function Method . . . . .	54
Comparison . . . . .	71
V. CONCLUSION AND FUTURE WORK . . . . .	85
Conclusion . . . . .	85
Future Work . . . . .	86
REFERENCES . . . . .	89

# LIST OF SYMBOLS

$a$	Speed of sound
$a_{mn}$	Coefficient in the approximation of the vibration modes
$b$	Wing semi-chord nondimensionalized by $C$
$C_p$	Pressure coefficient
$C_R$	Root chord
$C_z$	Normal force coefficient
$K$	Kernel
$k$	Reduced frequency ( $= \frac{\omega C_R}{2U_\infty}$ )
$l, m, n$	Coordinates of control points
$M$	Mach number
$P$	Lifting pressure
$P_w$	Weighting functions
$q$	Dynamic pressure ( $= \frac{1}{2} \rho U_\infty^2$ )
$s$	Wing semi-span
$U_\infty$	Free-stream velocity
$V$	Flow velocity vector ( $= V(x, y, z, t)$ )
$W$	Unnormalized normalwash
$w$	$W/U_\infty$
$\bar{w}$	Modal displacement
$x, y, z$	Coordinates of receiving points
$\alpha, \beta, \gamma$	Coordinates of load (integration) points

$\bar{a}, \bar{b}$	Coordinates of the load points in the transformed plane
$\Delta C_p$	Lifting pressure coefficient
$\xi, \eta, \zeta$	Coordinates of sending points
$\sigma$	Lateral coordinate in the plane of the surface
$\rho$	Density of air at sea level
$\phi$	Velocity potential ( $=\phi(x,y,z,t)$ )
$\omega$	Frequency of oscillation
$\lambda$	Sweep angle

## LIST OF FIGURES

<u>Figure</u>	<u>page</u>
1. Configuration of F-5 Wing . . . . .	10
2. Configuration of F-5 Wing with Stores . . . . .	11
3. Wing and Element Coordinates . . . . .	13
4. Idealization of Wing Panel into Boxes . . . . .	15
5. Coordinates of Transformed Surface . . . . .	20
6. Surface and Loading Types . . . . .	23
7. Various Tip Store Cross Sections . . . . .	25
8. Mode Shape of the Clean Wing ( $M=0.95$ , $F=20\text{Hz}$ , $\alpha=0$ ) .	27
9. Geometrical Model of Wing-Launcher (DLM) . . . . .	31
10. Geometrical Model of Missile (DLM) . . . . .	32
11. Geometrical Model of Wing-Launcher (KFM) . . . . .	33
12. Geometrical Model of Missile (KFM) . . . . .	34
13. Unsteady Lift Coefficient Distributions of Clean Wing . . . . .	38
14. Unsteady Lift Coefficient Distributions ( $M=0.6$ , $k=0.200$ , DLM, 22 Models) . . . . .	40
15. Unsteady Lift Coefficient Distributions ( $M=0.7$ , $k=0.173$ , DLM, 22 Models) . . . . .	41
16. Unsteady Lift Coefficient Distributions ( $M=0.8$ , $k=0.153$ , DLM, 22 Models) . . . . .	42
17. Unsteady Lift Coefficient Distributions ( $M=0.9$ , $k=0.138$ , DLM, 22 Models) . . . . .	43
18. Unsteady Lift Coefficient Distributions ( $M=0.6$ , $k=0.200$ , DLM, 8 Models) . . . . .	46

19.	Unsteady Lift Coefficient Distributions ( $M=0.7$ , $k=0.173$ , DLM, 8 Models) . . . . .	49
20.	Unsteady Lift Coefficient Distributions ( $M=0.8$ , $k=0.153$ , DLM, 8 Models) . . . . .	51
21.	Unsteady Lift Coefficient Distributions ( $M=0.9$ , $k=0.138$ , DLM, 8 Models) . . . . .	53
22.	Unsteady Lift Coefficient Distributions ( $M=0.6$ , $k=0.200$ , KFM, 6 Models) . . . . .	59
23.	Unsteady Lift Coefficient Distributions ( $M=0.7$ , $k=0.173$ , KFM, 6 Models) . . . . .	61
24.	Unsteady Lift Coefficient Distributions ( $M=0.8$ , $k=0.153$ , KFM, 6 Models) . . . . .	63
25.	Unsteady Lift Coefficient Distributions ( $M=0.9$ , $k=0.138$ , KFM, 6 Models) . . . . .	65
26.	Unsteady Lift Coefficient Distributions ( $M=1.1$ , $k=0.116$ , KFM, 6 Models) . . . . .	68
27.	Unsteady Lift Coefficient Distributions ( $M=1.35$ , $k=0.101$ , KFM, 6 Models) . . . . .	70
28.	Pressure Distributions at Section 2 (Real, $M=0.8$ , $k=0.153$ ) for Various Models . . . . .	76
29.	Pressure Distributions at Section 2 (Imag, $M=0.8$ , $k=0.153$ ) for Various Models . . . . .	77
30.	Pressure Distributions at Section 5 (Real, $M=0.8$ , $k=0.153$ ) for Various Models . . . . .	79
31.	Pressure Distributions at Section 5 (Imag, $M=0.8$ , $k=0.153$ ) for Various Models . . . . .	80
32.	Pressure Distributions at Section 8 (Real, $M=0.8$ , $k=0.153$ ) for Various Models . . . . .	82
33.	Pressure Distributions at Section 8 (Imag, $M=0.8$ , $k=0.153$ ) for Various Models . . . . .	83

# LIST OF TABLES

<u>Table</u>	<u>page</u>
1. Coefficients " $a_{mn}$ " for Various Vibration Modes . . .	37
2. Unsteady Lift Coefficient Distributions of Clean Wing . . . . .	37
3. Unsteady Lift Coefficient Distributions (Real, $M=0.6$ , $k=0.200$ , DLM, 8 Models) . . . . .	45
4. Unsteady Lift Coefficient Distributions (Imag, $M=0.6$ , $k=0.200$ , DLM, 8 Models) . . . . .	45
5. Unsteady Lift Coefficient Distributions (Real, $M=0.7$ , $k=0.173$ , DLM, 8 Models) . . . . .	48
6. Unsteady Lift Coefficient Distributions (Imag, $M=0.7$ , $k=0.173$ , DLM, 8 Models) . . . . .	48
7. Unsteady Lift Coefficient Distributions (Real, $M=0.8$ , $k=0.153$ , DLM, 8 Models) . . . . .	50
8. Unsteady Lift Coefficient Distributions (Imag, $M=0.8$ , $k=0.153$ , DLM, 8 Models) . . . . .	50
9. Unsteady Lift Coefficient Distributions (Real, $M=0.9$ , $k=0.138$ , DLM, 8 Models) . . . . .	52
10. Unsteady Lift Coefficient Distributions (Imag, $M=0.9$ , $k=0.138$ , DLM, 8 Models) . . . . .	52
11. Comparison of Effort ( $M=0.6$ , $k=0.200$ , DLM, 8 Models)	55
12. Comparison of Effort ( $M=0.7$ , $k=0.173$ , DLM, 8 Models)	55
13. Comparison of Effort ( $M=0.8$ , $k=0.153$ , DLM, 8 Models)	56
14. Comparison of Effort ( $M=0.9$ , $k=0.138$ , DLM, 8 Models)	56
15. Unsteady Lift Coefficient Distributions (Real, $M=0.6$ , $k=0.200$ , KFM, 6 Models) . . . . .	58
16. Unsteady Lift Coefficient Distributions (Imag, $M=0.6$ , $k=0.200$ , KFM, 6 Models) . . . . .	58

17.	Unsteady Lift Coefficient Distributions (Real, M=0.7, k=0.173, KFM, 6 Models)	60
18.	Unsteady Lift Coefficient Distributions (Imag, M=0.7, k=0.173, KFM, 6 Models)	60
19.	Unsteady Lift Coefficient Distributions (Real, M=0.8, k=0.153, KFM, 6 Models)	62
20.	Unsteady Lift Coefficient Distributions (Imag, M=0.8, k=0.153, KFM, 6 Models)	62
21.	Unsteady Lift Coefficient Distributions (Real, M=0.9, k=0.138, KFM, 6 Models)	64
22.	Unsteady Lift Coefficient Distributions (Imag, M=0.9, k=0.138, KFM, 6 Models)	64
23.	Unsteady Lift Coefficient Distributions (Real, M=1.1, k=0.116, KFM, 6 Models)	67
24.	Unsteady Lift Coefficient Distributions (Imag, M=1.1, k=0.116, KFM, 6 Models)	67
25.	Unsteady Lift Coefficient Distributions (Real, M=1.35, k=0.101, KFM, 6 Models)	69
26.	Unsteady Lift Coefficient Distributions (Imag, M=1.35, k=0.101, KFM, 6 Models)	69
27.	Comparison of Effort (M=0.6, k=0.200, KFM, 6 Models)	72
28.	Comparison of Effort (M=0.7, k=0.173, KFM, 6 Models)	72
29.	Comparison of Effort (M=0.8, k=0.153, KFM, 6 Models)	73
30.	Comparison of Effort (M=0.9, k=0.138, KFM, 6 Models)	73
31.	Comparison of Effort (M=1.10, k=0.116, KFM, 6 Models)	74
32.	Comparison of Effort (M=1.35, k=0.101, KFM, 6 Models)	74
33.	Pressure Distributions at Section 2 (Real, M=0.8, k=0.153) for Various Models	75
34.	Pressure Distributions at Section 2 (Imag, M=0.8, k=0.153) for Various Models	75
35.	Pressure Distributions at Section 5 (Real, M=0.8, k=0.153) for Various Models	78

- 36. Pressure Distributions at Section 5 (Imag,  $M=0.8$ ,  
 $k=0.153$ ) for Various Models . . . . . 78
- 37. Pressure Distributions at Section 8 (Real,  $M=0.8$ ,  
 $k=0.153$ ) for Various Models . . . . . 81
- 38. Pressure Distributions at Section 8 (Imag,  $M=0.8$ ,  
 $k=0.153$ ) for Various Models . . . . . 81



## Chapter I

### INTRODUCTION

When large external bodies or stores, such as missiles, bombs, or fuel tanks, are added to the wings of an airplane, the dynamic characteristics of the aircraft will be changed. In particular, the flutter speed of the aircraft may be significantly affected because of the inertial, elastic, and aerodynamic interaction between the wing and its mounted stores. Thus, theoretical aeroelasticity is essential for the flutter evaluation of this type of airplanes.

However, until recently, the computation of aerodynamic loadings over complex geometric configurations was not possible. Fortunately, the development of three-dimensional aerodynamic codes capable of calculating wing-body interaction has now advanced to the point where the flow about these complex structures and thus the aerodynamic forces and pressures can be predicted quite accurately. In order to achieve this accuracy, rather detailed models have to be established.

### 1.1 BACKGROUND

Several recent studies and tests have considered the effects of store aerodynamics on unsteady wing airloads with emphasis placed on wings with tip missiles.

Chadwick (1) presented a nonplanar lifting surface theory to predict sideloads on underwing pylon store models. The wing pylon model was limited to incompressible flow and slender body theory was used to model the store. Kraus (2) used panel methods to compute forces and moments on external stores mounted underneath an F-4 wing in subsonic flow. Martin, Saunders, and Smith (3) reported an analysis of the aerodynamic interference problem for external aircraft stores by use of the image system technique. The stores were assumed to be slender, axisymmetric bodies and the interference was analyzed by first assuming a cross-flow solution. In the Netherlands, Roos, Bennekens, and Zwaan (4) of NLR described a panel method for the calculation of aerodynamic loadings on harmonically oscillating wing/body configurations in subsonic flow. The loads on the body were represented by an unsteady source panel distribution, while the unsteady aerodynamic forces on the lifting surfaces were computed by the doublet lattice method. A wing/tip tank and a pylon/store configuration were evaluated. Parker (5) used the doublet lattice method together with the method of images to predict unsteady aerodynamic coefficients and pressures for an F-5 wing with various store configurations

oscillating in subsonic flow. A variety of finite element lattice configurations was evaluated for numerical convergence. Cenko, Tinoco, Dyer, and DeJongh (6) analyzed the complex flow associated with aircraft/weapons carriage and mutual interference during store separation by means of the PAN AIR code. This program is based on a higher order panel method. Dusto (7) also presented a higher order paneling method to compute steady and unsteady flows about an F-5 wing with and without underwing and wingtip store. These results and similar ones from another higher order panel method and a doublet lattice method were compared by Sotomayer, Dusto, Epton, and Johnson (8) to experimental results for the same configurations from NLR (9). In a wing/store flutter suppression investigation, Noil, Huttshell, and Cooley (10) used the subsonic doublet lattice option in the automated flutter analysis module of the FASTOP program (11) to perform unaugmented flutter calculations, and to obtain unsteady aerodynamic forces for a YF-17 wing with an AIM-7S missile mounted on an outboard wing pylon and with an empty launcher rail. Pollock, Sotomayer, Huttshell, and Cooley (12) evaluated various methods for the predictions and prevention of wing/store flutter. The measured aerodynamic data of the NLR experiments were compared to unsteady aerodynamic data from a paneling method by Woodward (13). Flutter analyses were performed using the doublet lattice module in the flutter

code FACES (14) for the same configurations. Triplett (15) used doublet lattice theory to evaluate the effect of detailed aerodynamic modeling of the F/A-18 wing with underwing stores and tip missile. He presented results showing the effect of individual system components on flutter. Finally, Turner (16) presented an analytical study of the effect of store aerodynamics on wing/store flutter by using multivariate analysis techniques.

In all this above mentioned research, the pylon/store or launcher/store configurations were modeled in three-dimensional detail. For an applied flutter analysis in the flutter certification of aircraft with stores, this becomes very costly, as pointed out by Turner.

## 1.2 SCOPE OF PRESENT RESEARCH

The computations of the unsteady aerodynamic coefficients for an aircraft are the single most costly item in any flutter analysis. Also, owing to the variety of stores that can be carried on typical modern tactical military aircraft, the total number of possible aircraft/store configurations is rather large. Thus, with thousands of flutter computations to be performed, the cost becomes prohibitive.

In many cases, this increased cost is not justified because store aerodynamics tend to have a small effect on flutter speed as shown by Turner (16). However, there are

important instances where neglecting store aerodynamics will lead to a dangerous over-estimation of flutter speed. Determination when store aerodynamics should be included in the flutter analysis is a major problem.

As a compromise it has become common practice to model the stores solely as flat plates when computing the aerodynamic loads on oscillating wing-body combinations. This, however, tends to reduce the accuracy of the results.

According to Chapman (17), for panel methods the computation time varies with the number of panels  $n$  as somewhere between  $n^2$  and  $n^3$ . Thus, a compromise has to be sought between the complex geometric modeling in a one-time evaluation of a computer code and the requirement for simplicity of the model to save cost in repeated flutter analyses of multiple aircraft/store configurations, while also preserving sufficient accuracy.

In this investigation, studies are conducted to evaluate various geometric models for pylons and stores such as endplates, endplate - flat plate combinations, and these models at various dihedral angles, in comparison to the computational flat plate models now in use. This is done with respect to complexity and accuracy using a kernel function code, ANKF, by Cunningham (18) and a doublet lattice code, H7WC, by Giesing, Kalman, and Rodden (19) to investigate whether the accuracy of the aerodynamic results can be increased by using these somewhat more complex models

without having to pay the high price for very detailed models.

A comparison to experimental results for the F-5 wing with tip mounted stores obtained by NLR (9) is performed as well as a comparison to computational results of the same wing, obtained for very detailed store models, by Sotomayer, Dusto, Epton, and Johnson (8), who utilized higher order paneling methods and by Parker (5), who used the doublet lattice method.

## Chapter II

### DEVELOPMENT OF THEORY

Steady and unsteady aerodynamic loads on airplanes are used, in general, to analyze flutter, gust, and frequency response as well as for the computation of static and dynamic stability derivatives. Thus, the accurate and efficient prediction of these aerodynamic loads is an essential requirement for any such analysis.

The use of lifting surface theory has been the classic way to solve the unsteady compressible flow problem. Starting from conservation of mass, momentum, and energy as well as from Gibb's thermodynamics, for an inviscid and adiabatic fluid under the assumptions of irrotationality as well as that of potential flow, the governing equation for the unsteady aerodynamic theory is given by a form of the wave equation:

$$\nabla^2 \phi - \frac{1}{a^2} \left[ \frac{\partial^2 \phi}{\partial t^2} + \frac{\partial(V^2)}{\partial t} + V \cdot \nabla \left( \frac{V^2}{2} \right) \right] = 0 \quad (2.1)$$

where  $\phi$  is the velocity potential,  $V$  is the flow velocity vector, and  $a$  is the speed of sound. Assuming harmonic

motion and using linear superposition of singularities on the wing, the solutions to this equation can be written in integral form as a relationship between the velocity normal to the wing and the pressure on the wing.

Two basic classes of lifting surface theories now widely used are the kernel function method in its traditional form and the doublet lattice method which represents a finite element technique.

In the kernel function method, assumed pressure functions are required as input to these solutions and the unknowns are the coefficients associated with these pressure functions.

The finite element methods do not require assumed pressure functions as input to obtain a solution. This advantage, however, is offset by the fact that the cost per solution is much higher, as the finite element method requires a very fine mesh and thus a large number of elements to converge to an acceptable solution.

On the other hand, if special weighting functions are used in the assumed pressure distributions with implicit discontinuous characteristics, the kernel function method can show a much faster rate of solution convergence than the finite element method. It is, thus, obvious that the kernel function method can have an economic advantage over finite element methods.



To investigate an F-5 wing (Figure 1) with a tip mounted launcher and AIM-7S missile (Figure 2) in unsteady flow, the studies herein were conducted by using a kernel function code (ANKF) for subsonic and supersonic flow and a doublet lattice code (H7WC) for only subsonic flow.

## 2.1 DOUBLET LATTICE METHOD

### 2.1.1 Introduction

To account for the interference between a body (such as a fuselage) and a wing and between a wing (such as a stabilizer) and a wing, lifting surface finite elements which are not necessarily planar are applied to both the body surfaces and lifting surfaces in this method. Here, any body is regarded as an annular wing as was used by Woodward (13) in his study of the steady case. This method calculates lift distributions on surfaces in steady and oscillatory motion, even in the case of nonplanar surface configuration, at only subsonic speeds.

The doublet lattice method is simple, accurate, and very versatile. An overview of the developments of the steady and unsteady doublet lattice methods is given in the paper by Giesing, Kalman, and Rodden (20).

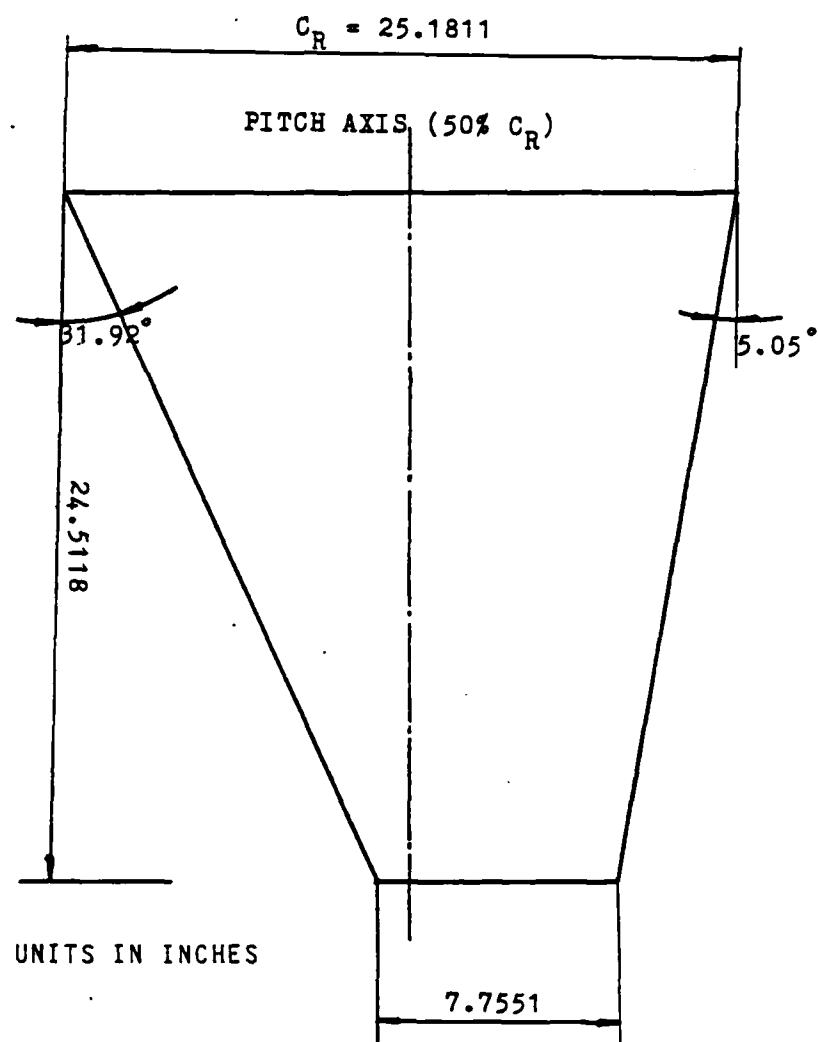


Figure 1: Configuration of F-5 Wing

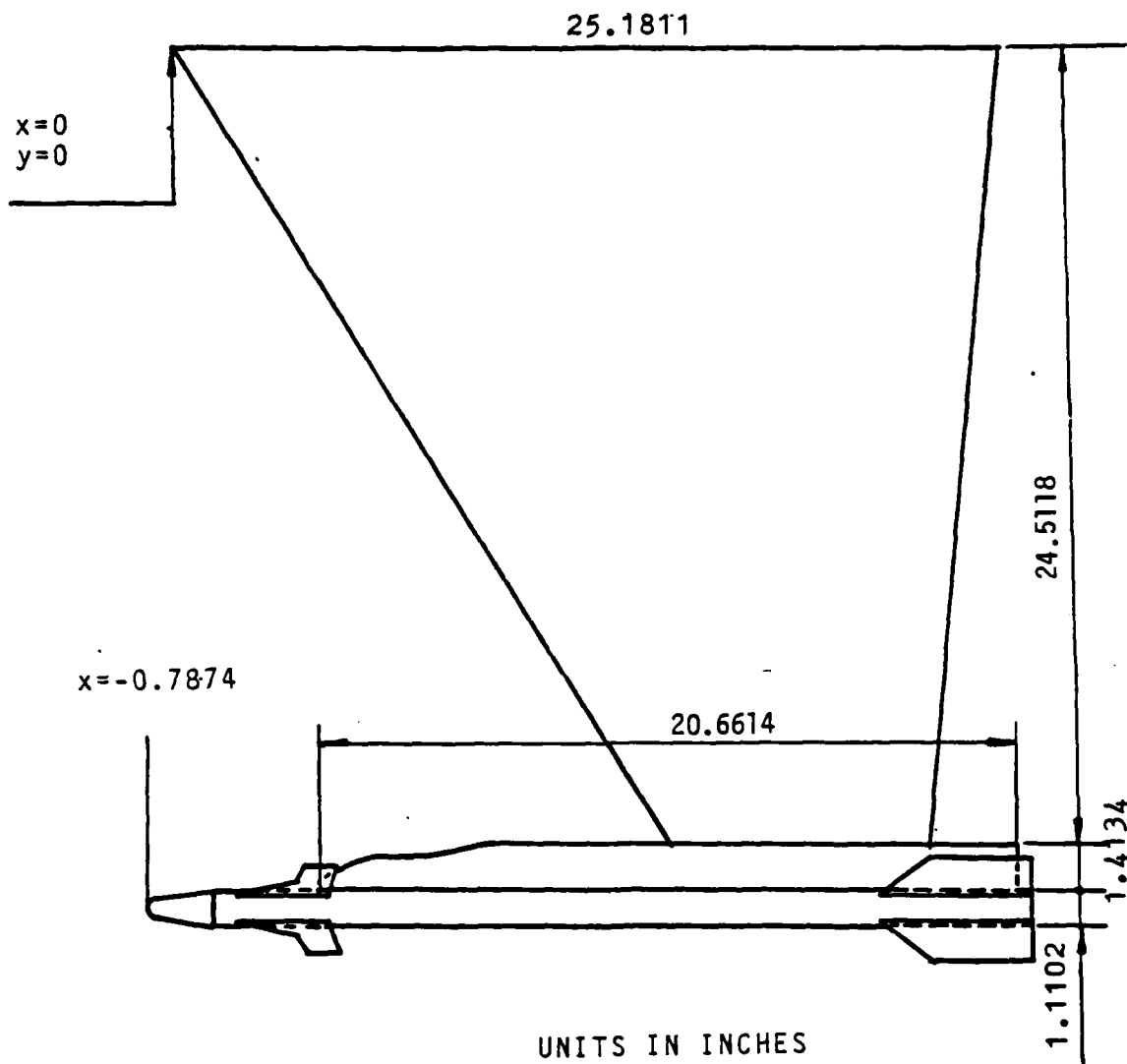


Figure 2: Configuration of F-5 Wing with Stores

### 2.1.2 Theoretical Development

The forces exerted on a wing depend on the velocity components of the air stream. These are the velocity of the free stream  $U_\infty$  which is opposite to the direction of motion, and the velocity  $W$  which is perpendicular to the direction of motion. Here, the velocity normal to an oscillating surface,  $W$ , can be calculated from the equation

$$W = U_\infty \operatorname{Re}(w e^{i\omega t}) \quad (2.2)$$

where

$$w(x, y, z) = \frac{1}{8\pi} \iiint_{\text{L.S.}} K(x-\xi, y-\eta, z-\zeta, \omega, M) \Delta C_p d\xi d\sigma \quad (2.3)$$

where  $\xi$  is the streamwise coordinate,  $\sigma$  is the tangential spanwise coordinate (Figure 3), and  $\omega$  is the frequency of the oscillation.  $K()$  is the kernel,  $M$  is the Mach number, and  $\Delta C_p$  is the lifting pressure coefficient which can be expressed in terms of lifting pressure and dynamic pressure as follows:

$$\Delta C_p = \frac{P_{\text{lower}} - P_{\text{upper}}}{q}$$

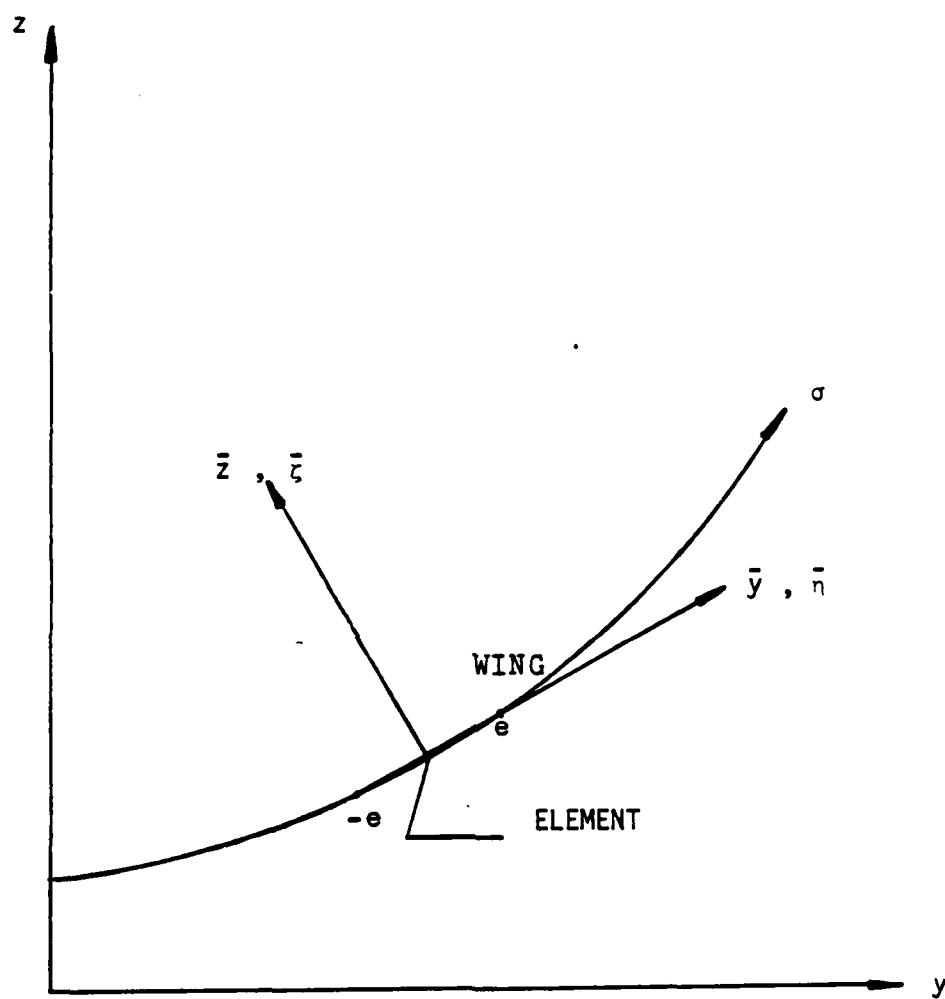


Figure 3: Wing and Element Coordinates

In the integration, the functions are integrated over all of the lifting surfaces.

Since the doublet lattice method applies the lifting surface finite elements over all the body surfaces and the wing surfaces, the above integration can be written as follows:

$$w(x,y,z) = \frac{1}{8\pi} \sum \Delta C_{ps} \iint_{\text{Element}_s} K(x-\xi, y-\eta, z-\zeta, \omega, M) d\xi d\sigma \quad (2.4)$$

where subscript s indicates the sending elements of the surfaces.

The basic concept of the doublet lattice method, which determines the influence of an oscillating lifting surface element at a point, assumes that the lifting pressure could be concentrated along a line. This line is located at the 1/4 chord line of the sending element (Figure 4). Here, the steady flow effect is modeled by a horseshoe vortex which is located in each element with its bound leg along this 1/4 chord line. Additionally, the unsteady flow effect is modeled by a uniform line of acceleration potential doublets which is superimposed onto the bound vortex. Thus, both vortex and doublet effects are represented by an influence function which relates the pressure amplitude and the normalwash amplitude at a given control point. Therefore, the first step of the procedure requires the dividing of the

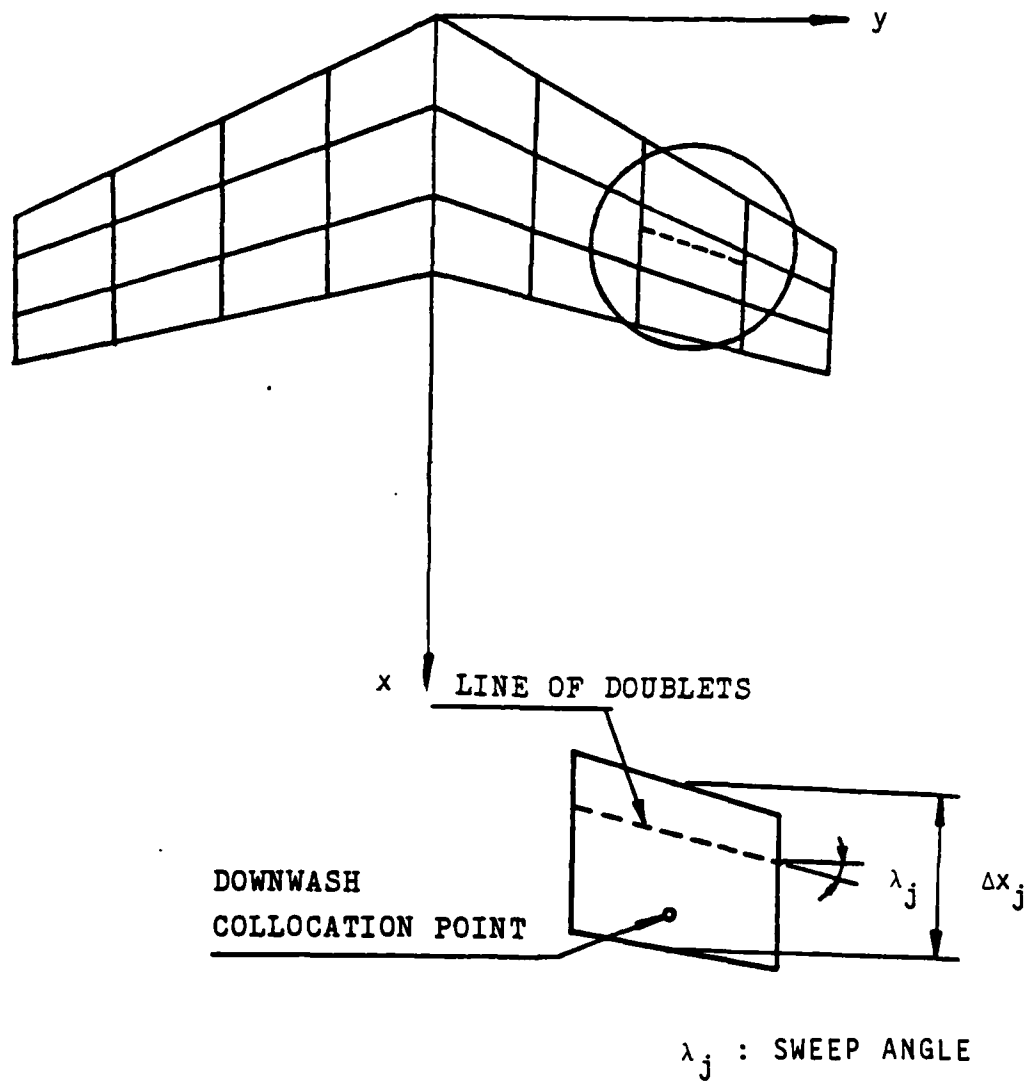


Figure 4: Idealization of Wing Panel into Boxes

lifting surfaces into small boxes (elements) which are oriented in strips parallel to the free stream. Moreover, it is advantageous to align any surface edges, hinge lines, and fold lines with the boundaries of the elements. Then, the integral equation (2.4) can be rewritten as follows:

$$w(x,y,z) = \sum_{\text{Element}_s} \Delta C_{ps} \frac{\Delta \xi}{8\pi} \int K(x-\xi_1/4, y-\eta, z-\zeta, \omega, M) d\sigma \quad (2.5)$$

In this equation, the normalwash boundary condition  $w(x,y,z)$  is known, but the lifting pressure coefficient  $\Delta C_p$  over each element is unknown.

James (21) used a control point (or receiving point) at which the normalwash boundary condition is satisfied on each element. He located this point at the center in spanwise direction on the 3/4 chord line of each element. For a two-dimensional case, he showed that this location gave highly accurate results and was considered to be optimum for the doublet lattice method.

Therefore, in order to calculate the unknown values of  $\Delta C_p$ , we can write equation (2.5) in matrix form:

$$\{ w \} = [ D ] \{ \Delta C_p \} \quad (2.6)$$



where the elements of the normalwash factor matrix  $[D]$  are given as

$$D = \int_{\text{Element}_s} K(x-\xi_1/4, y-\eta, z-\zeta, \omega, M) d\sigma \quad (2.7)$$

In general, we solve this matrix equation by inverting the matrix  $[D]$  as follows:

$$\{ \Delta C_p \} = [D]^{-1} \{ w \} \quad (2.8)$$

However, when the matrix  $[D]$  is large, it is not easy and not efficient to calculate its inverse. Therefore, the present method solves the linear simultaneous equations (2.6) by direct Gaussian Triangularization and back solution. Due to this fact, the present doublet lattice method has the disadvantage that additional problems can only be solved by repeating the whole procedure of triangularization and back solution.

## 2.2 KERNEL FUNCTION METHOD

### 2.2.1 Introduction

While the doublet lattice method can only calculate the subsonic flow case, the kernel function method can be applied not only to the uniform and non-uniform subsonic

flow case, but also to the transonic, and supersonic flow cases. Moreover, we can apply local Mach number distributions over the lifting surfaces in this method, and include the dynamic effects of the components of the lifting surfaces and the external stores.

This method uses assumed pressure functions to solve the linear lifting surface problem with interference in steady or oscillating flow. Since, in the assumed pressure functions, a special weighting function is used to imply the discontinuous characteristics of the pressure distributions, the solution converges faster than is possible with the conventional pressure functions composed of smooth functions. This, however, also presents the greatest difficulty in the use of this method since proper assumptions have to be made for selecting the pressure functions. Details of the kernel function method are presented by Cunningham in Reference 18.

### 2.2.2 Theoretical Development

As in the doublet lattice method, the forces experienced by the surfaces are related to the downwash which is the velocity normal to the lifting surface. The relationship between downwash and pressure can be expressed as follows:

$$w(l,m,n) = \frac{1}{4\pi\rho U_\infty} \sum \int \Delta P(\alpha,\beta,\gamma) K(l-\alpha,m-\beta,n-\gamma,k,M) ds \quad (2.9)$$

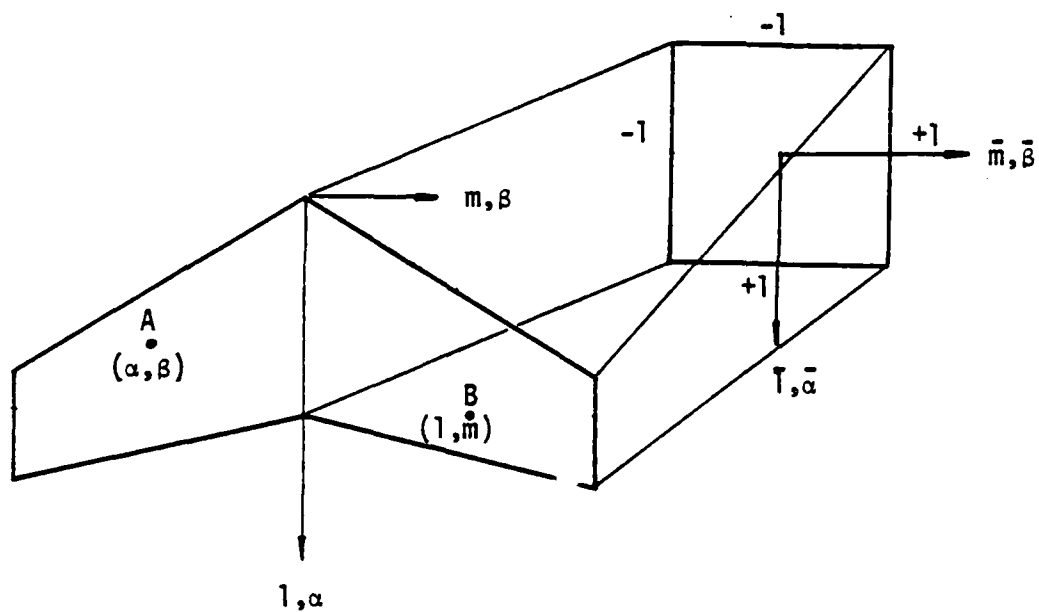
where the downwash  $w(l,m,n)$  is the normal velocity at control point  $(l,m,n)$ , and the function  $\Delta P(\alpha, \beta, \gamma)$  is the normal pressure distribution on the lifting surface at a load (or integration) point.  $K()$  is the kernel function,  $k$  is the reduced frequency, and  $M$  is the Mach number.

In equation (2.9), while the downwash  $w(l,m,n)$  is a known quantity and is given by the boundary conditions on the respective lifting surfaces as depending on the mode shape and the frequency of oscillation,  $\Delta P(\alpha, \beta, \gamma)$  is unknown. Therefore, to solve this equation by the present method, the unknown pressure functions are assumed to be a set of chordwise and spanwise polynomials with weighting functions. The form of the assumed pressure functions is as follows:

$$\Delta P(\bar{\alpha}, \bar{\beta}) = q P_w(\bar{\alpha}, \bar{\beta}) [ g_0(\bar{\beta}) f_0(\bar{\alpha}) + g_1(\bar{\beta}) f_1(\bar{\alpha}) + \dots ] \quad (2.10)$$

where the coordinates  $\bar{\alpha}$  and  $\bar{\beta}$  are defined in the transformed plane of the surface (Figure 5), and  $q$  is the freestream dynamic pressure. Here, the chordwise functions,  $f_n(\bar{\alpha})$ , are

$$\begin{aligned} f_0(\bar{\alpha}) &= U_0(\bar{\alpha}) = 1 \\ f_1(\bar{\alpha}) &= U_1(\bar{\alpha}) + U_0(\bar{\alpha}) = 2\bar{\alpha} + 1 \\ &\vdots \\ f_n(\bar{\alpha}) &= U_n(\bar{\alpha}) + U_{n-1}(\bar{\alpha}) \end{aligned} \quad (2.11)$$



A : INTEGRATION POINT

B : DOWNWASH POINT

Figure 5: Coordinates of Transformed Surface

and the spanwise functions,  $g_m(\bar{\beta})$ , are expressed as

$$g_m(\bar{\beta}) = [ a_{m0} U_0(\bar{\beta}) + a_{m1} U_1(\bar{\beta}) + \dots ] \quad (2.12)$$

where the coefficients "a"s are the unknowns and  $U_n(\ )$  are the Tschetchev polynomials of the second kind:

$$\begin{aligned} U_0(\bar{\beta}) &= 1 \\ U_1(\bar{\beta}) &= 2\bar{\beta} \\ &\vdots \\ &\vdots \\ &\vdots \\ U_n(\bar{\beta}) &= 2\bar{\beta}U_{n-1}(\bar{\beta}) - U_{n-2}(\bar{\beta}) \end{aligned} \quad (2.13)$$

In equation (2.10), the function  $P_w(\bar{\alpha}, \bar{\beta})$  is the weighting function which depends on the pressure types in both chordwise and spanwise directions as shown in Figure 6, and on the speed of the flow at the downwash point.

If the downwash point is subsonic, a subsonic weighting function is used. Similarly, if the downwash point is supersonic, a supersonic weighting function may be used to calculate the downwash and the interference effect. In this report, the function  $P_w(\bar{\alpha}, \bar{\beta})$  was assumed as follows:

$$P_w(\bar{\alpha}, \bar{\beta}) = \frac{4\rho U_\infty^2}{b(\bar{\beta})} \text{sh}(\bar{\alpha}) I(\bar{\beta}) \quad (2.14)$$

and was used regardless of Mach number for subsonic, transonic, and supersonic solutions. Additional discussions about a supersonic weighting function are given in Reference 18 .

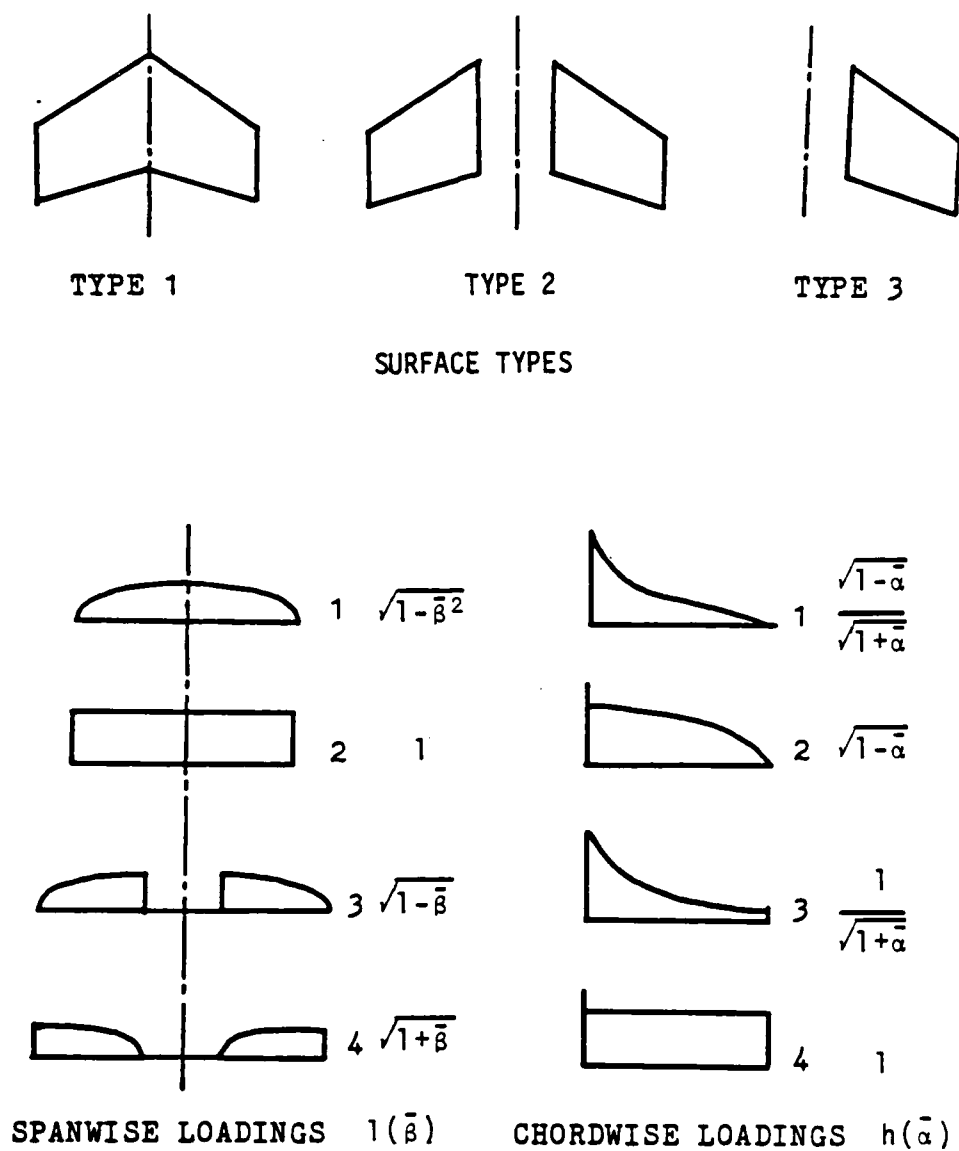


Figure 6: Surface and Loading Types

### Chapter III

#### NUMERICAL MODELING

In order to model the wing with tip mounted launcher and missile, it was assumed that the wing and launcher be flat plates. The dimensions of the wing were the same as in the NLR experiments where a slightly modified halfmodel of the outer part of the F-5 wing (scale 1:4.5) was used. The missile was simplified without fins as

- (1) a flat plate for accuracy evaluation
- (2) an endplate
- (3) various flat plate - endplate combinations  
to account for cross flow and pressure drop
- (4) an octagonal cylinder open at both ends
- (5) an axisymmetric slender body  
(for the doublet lattice method only)

For case 3, various cross sections were considered (Figure 7), and for case 4, a cylinder was idealized as having an octagonal shape with eight lifting surfaces. It is obvious that case 4 needs a large number of elements thus increased the computer cost.

For both, doublet lattice and kernel function computational methods, symmetric flow with respect to the



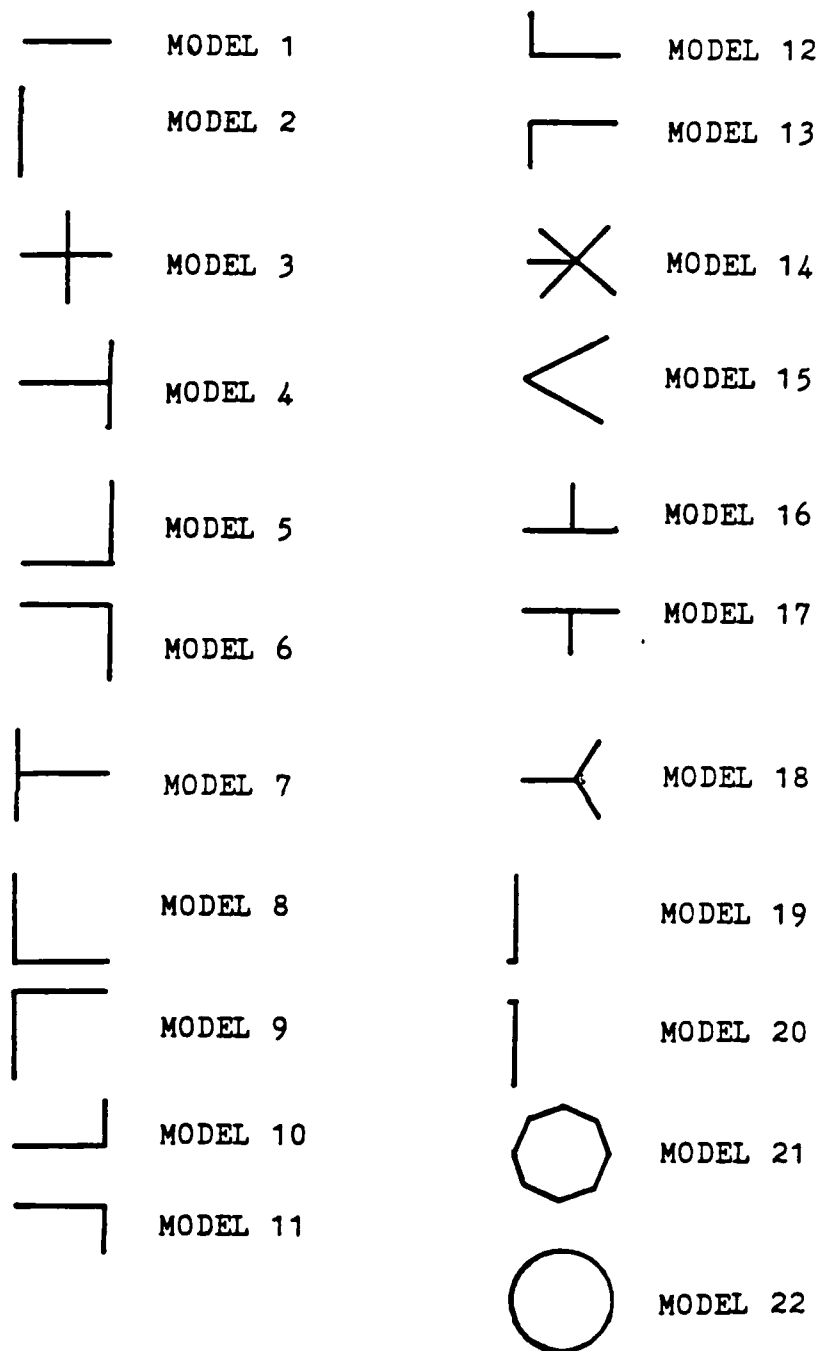


Figure 7: Various Tip Store Cross Sections

x-axis of the wing was assumed and the Mach number was assumed to be uniformly distributed over the wing surface.

To calculate the vibration modes of the wing and store, the following polynomial expression was taken from Reference 9:

$$\bar{w}(x,y) = \sum a_{mn} x^n y^m$$

wing : m=0,1,2    n=0,1

store : m=0            n=0,1

This expression assumes linear displacements in chordwise direction and parabolic displacements in spanwise direction. The coefficients  $a_{mn}$  are shown in Table 1 for several Mach numbers. In the experiments, the wing model was oscillated in pitch about a 50% root chord axis at varying frequencies.

A sample mode shape for the clean wing as used for the computation of the normalwash boundary conditions in the unsteady flow case at  $M=0.95$ ,  $F=20\text{Hz}$ , and  $\alpha=0$  is exhibited in Figure 8. The displacements are magnified to better show the deflection shape.

In this paper, a Mach number range between 0.6 and 1.35 is covered while the frequency of oscillation of the wing is kept at 20Hz. Generally, when the frequency is increased, the imaginary component of the lift increases but the real part of the lift decreases very slightly at constant Mach

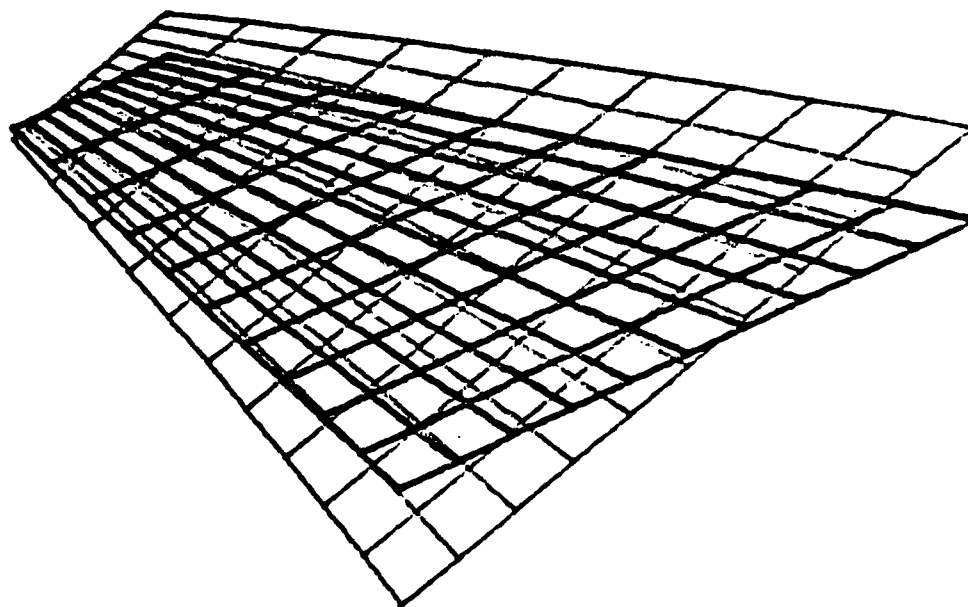


Figure 3: Mode Shape of the Clean Wing ( $M=0.95$ ,  $F=20\text{Hz}$ ,  $\alpha=0$ )

number. When the Mach number is increased without varying the frequency, the real component of the lift is increased while the imaginary component is decreased.

It was assumed that the lower surface and upper surface of the wing have the same aerodynamic characteristics for simplicity. The geometric characteristics of the wing are as follows:

Reference Area	=	0.26045	m <sup>2</sup>	( 403.7	in <sup>2</sup> )
Reference Chord	=	0.4183	m	( 16.4685	in )
Reference Semispan	=	0.6226	m	( 24.5118	in )
Wing Section		% Span			
1		18.1			
2		35.2			
3		51.2			
4		64.1			
5		72.1			
6		81.7			
7		87.5			
8		97.7			

Here the wing sections were chosen the same as those of the NLR experiments in order to compare computational and experimental results.

### 3.1 DOUBLET LATTICE METHOD

The model used for the doublet lattice method is shown in Figure 9 . The wing is formed by 11 strips which are subdivided into 10 chordwise elements or boxes. The launcher is idealized by 2 strips which have 16 boxes or elements in chordwise direction each. Since our main concern is the wing tip section, more elements have been located in that area. The tip-missile model is shown in Figure 10 . The flat panel which represents the missile model consists of 2 strips with a total of 19 boxes each. The width of the plate for the missile model is equal to the diameter of the actual missile. For this method only, a cylindrical axisymmetric slender body model was also used.

It should be mentioned here again that this method can only be applied to subsonic flow.

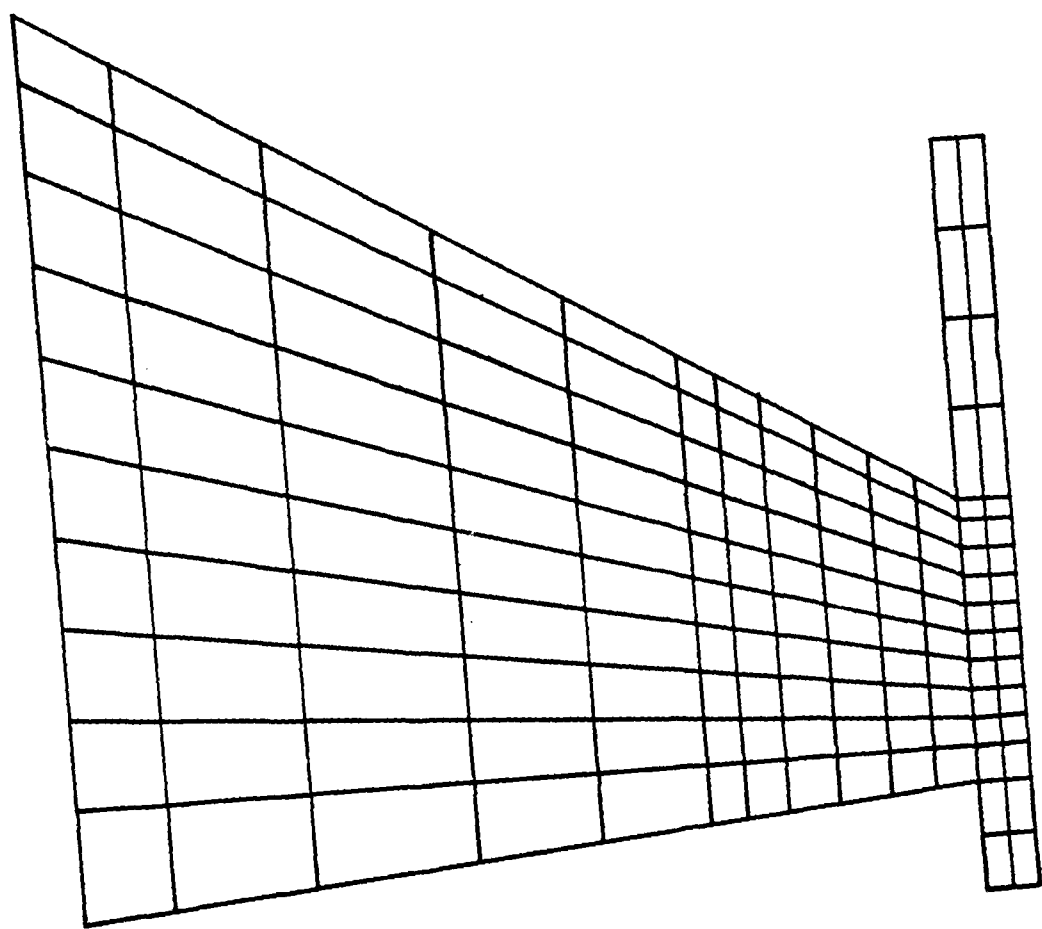
### 3.2 KERNEL FUNCTION METHOD

The model used for the kernel function method is similar to the doublet lattice model. Instead of boxes, it has structural points at which mode deflections are given. There are 88 structural points on the wing, 19 structural points on the launcher, and 11 structural points on the interface of wing and launcher (Figure 11).

The modeling of the tip-missile is almost the same as for the doublet lattice case. There are 21 structural points on the flat-panel modeled missile, and 18 interface

structural points between launcher and tip-missile (Figure 12). For this method, supersonic cases can be analyzed additionally but the slender body model cannot be used.

The spanwise loading of the wing was assumed to be of type 2 in Figure 6 and the surface to be of type 1. For the launcher, a spanwise loading of type 2 and the surface type 3 were used. Various different surface and loading types were used for the missile depending on the shape of the model. The chordwise loadings of wing, launcher, and missile were assumed to be of type 1.



<u>PANEL</u>	<u>STRIPS</u>	<u>BOXES</u>
WING	1 - 11	1 - 110
LAUNCHER	12 - 13	111 - 142

Figure 9: Geometrical Model of Wing-Launcher (DL4)

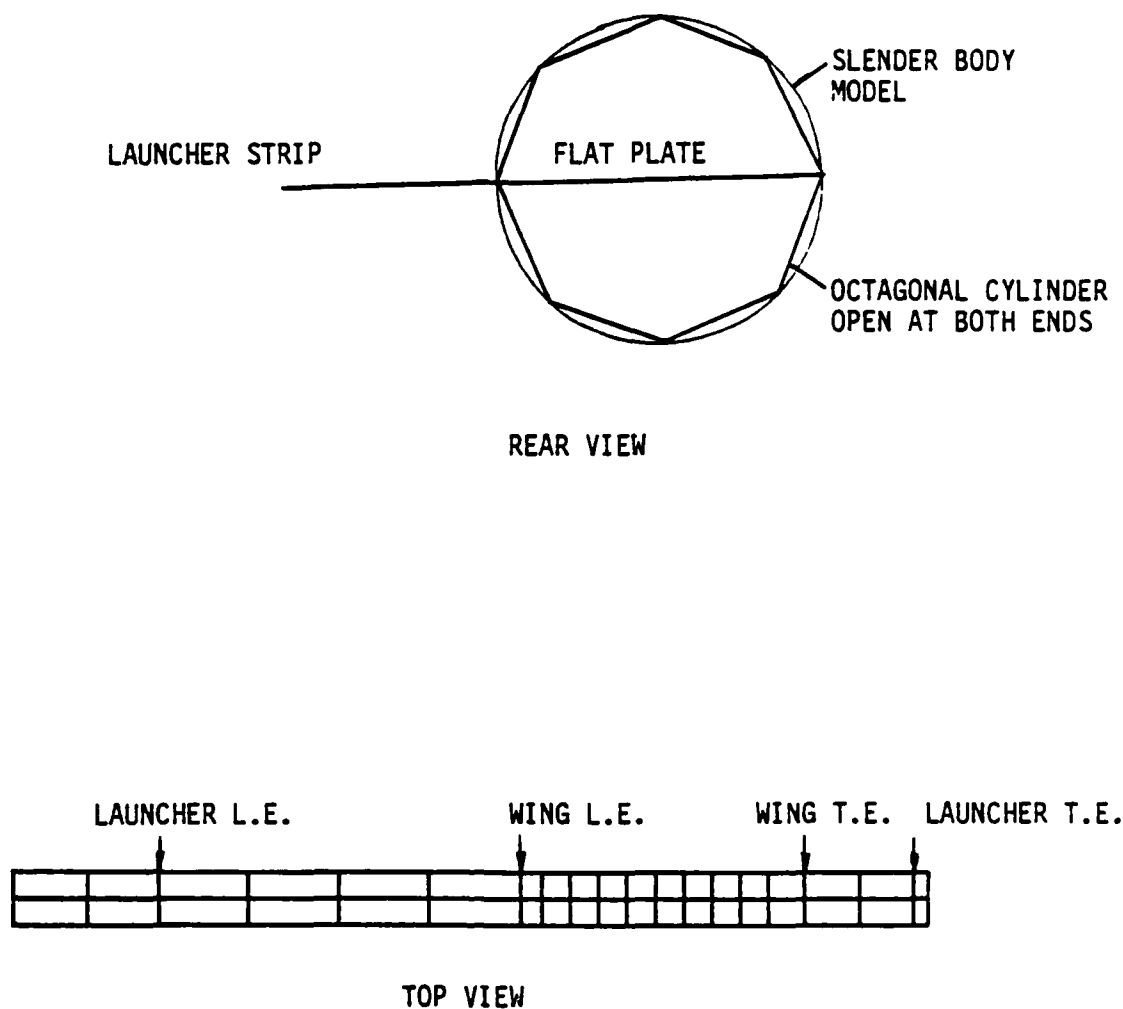
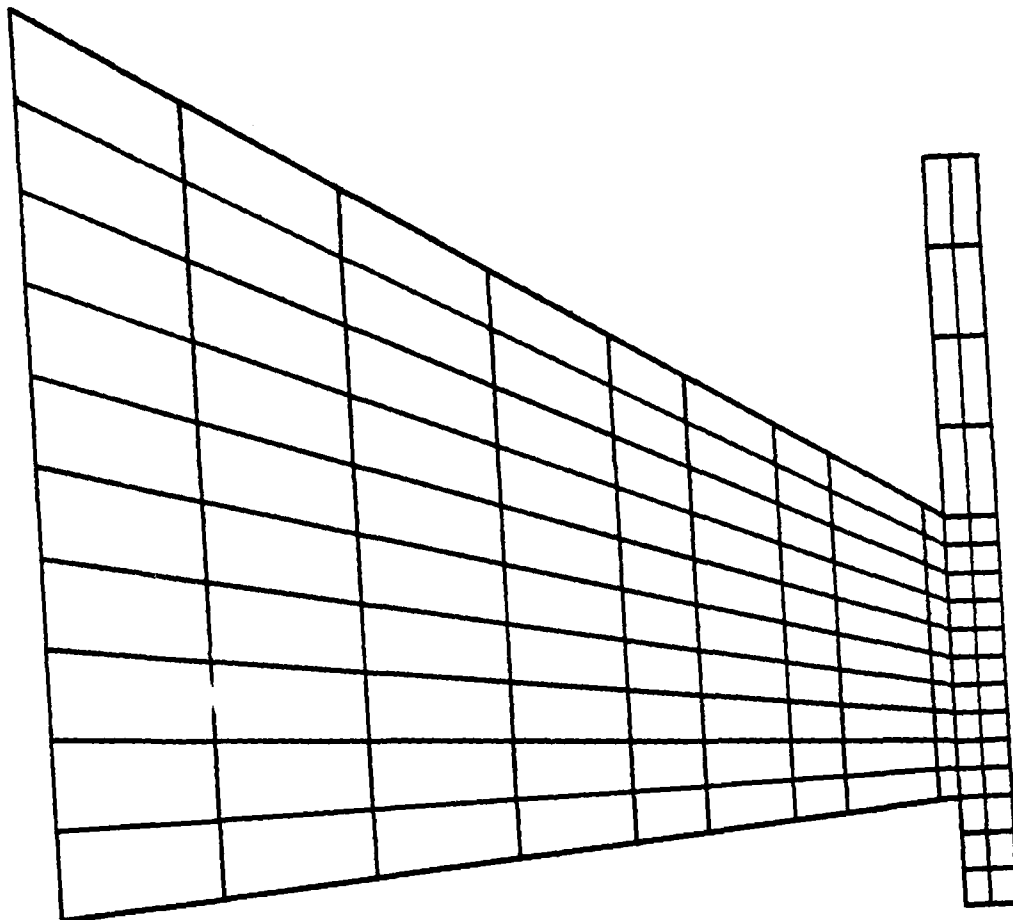


Figure 10: Geometrical Model of Missile (DLM)





<u>PANEL</u>	<u>STRUCTURAL POINTS</u>
WING	1 - 99
LAUNCHER	89 - 117
INTERFACE	89 - 99

Figure 11: Geometrical Model of Wing-Launcher (KFM)

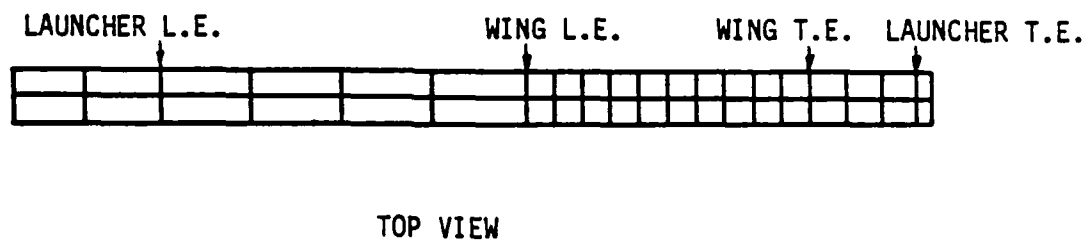
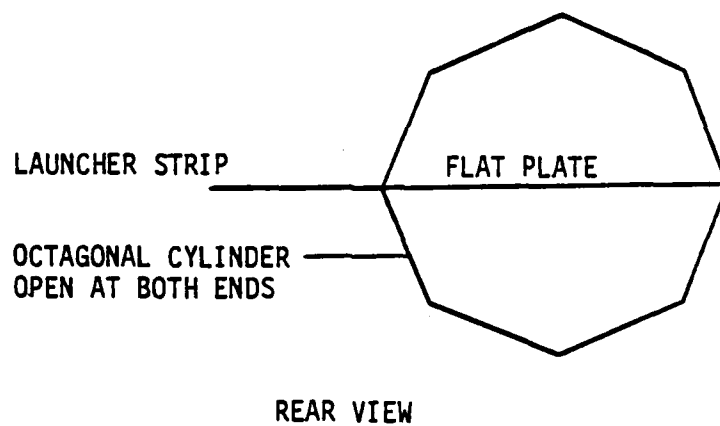


Figure 12: Geometrical Model of Missile (KFM)

## Chapter IV

### RESULTS

In all cases, the wing was oscillated about a near zero mean angle of incidence. Thus, the unsteady results are based on the total unsteady pressure difference between upper and lower surfaces.

Only curves for the lift coefficient distributions over the wing are presented since the moment coefficient distributions depend on the location of the elastic axis of the wing and can be computed by direct integration of the pressures over the wing. Lift and pressure coefficients for the various store models were obtained but are not given here since they are very small and vary widely between the different models. Also, no steady results are presented, since the assumption of the wing as a flat plate without camber and thickness does not yield agreeable results.

#### 4.1 CLEAN WING CASE

Before analyzing the characteristics of the various tip-store models, it is necessary to verify both computer codes by computing unsteady clean wing results and comparing these to existing results such as those of Parker and the experimental results of NLR.

The clean wing was analyzed in subsonic flow,  $M=0.6$ , and at a frequency of oscillation of  $F=20\text{Hz}$ . As evident in Figure 13 and Table 2, the unsteady lift coefficient distributions from the doublet lattice method (DLM) and from Parker exhibit good agreement, especially at the root and tip sections of the wing. It is believed that the discrepancy between the present DLM and Parker at 60%-90% of the span of the wing might have resulted from different vibration mode coefficients.

The results from the kernel function method show a slightly different shape than the two others. Here, the lift coefficient distribution presents higher values than the other two methods from the root section to mid-span. From mid-span to the tip-section, the lift coefficient drops off faster than for the other methods, but it is still close to both, the present DLM's and Parker's results.

All three sets of results show values 10%-15% higher than the experimental results from NLR. This might be due to the fact that no fuselage-wing interaction is considered nor is the wing-tip upwash condition being accounted for.

TABLE 1

Coefficients " $a_{mn}$ " for Various Vibration Modes

		M=0.6 k=0.200	M=0.7 k=0.173	M=0.8 k=0.153	M=0.9 k=0.133
Wing	a00	-0.336	-0.346	-0.351	-0.349
	a01	0.997	1.020	1.022	1.016
	a10	0.045	0.127	0.162	0.082
	a11	0.032	-0.260	-0.296	-0.209
	a20	-0.141	-0.400	-0.531	-0.442
	a21	-0.001	0.596	0.677	0.424
Tipstore	a00	-0.389	-0.450	-0.459	-0.513
	a01	1.022	1.099	1.075	1.098

TABLE 2

Unsteady Lift Coefficient Distributions of Clean Wing

Wing Span (%)	Parker	D.L.M	Error (%)	ANKF	Error (%)
9.75	1.04	1.04	0.00	1.08	3.85
29.89	1.16	1.17	0.36	1.20	3.45
46.91	1.27	1.28	0.79	1.31	3.15
63.13	1.36	1.38	1.47	1.37	0.74
76.92	1.38	1.41	2.17	1.38	0.00
87.76	1.30	1.34	3.08	1.24	-4.52
95.23	1.06	1.09	2.83	0.83	-21.70
99.04	0.67	0.69	2.99	0.49	-26.87

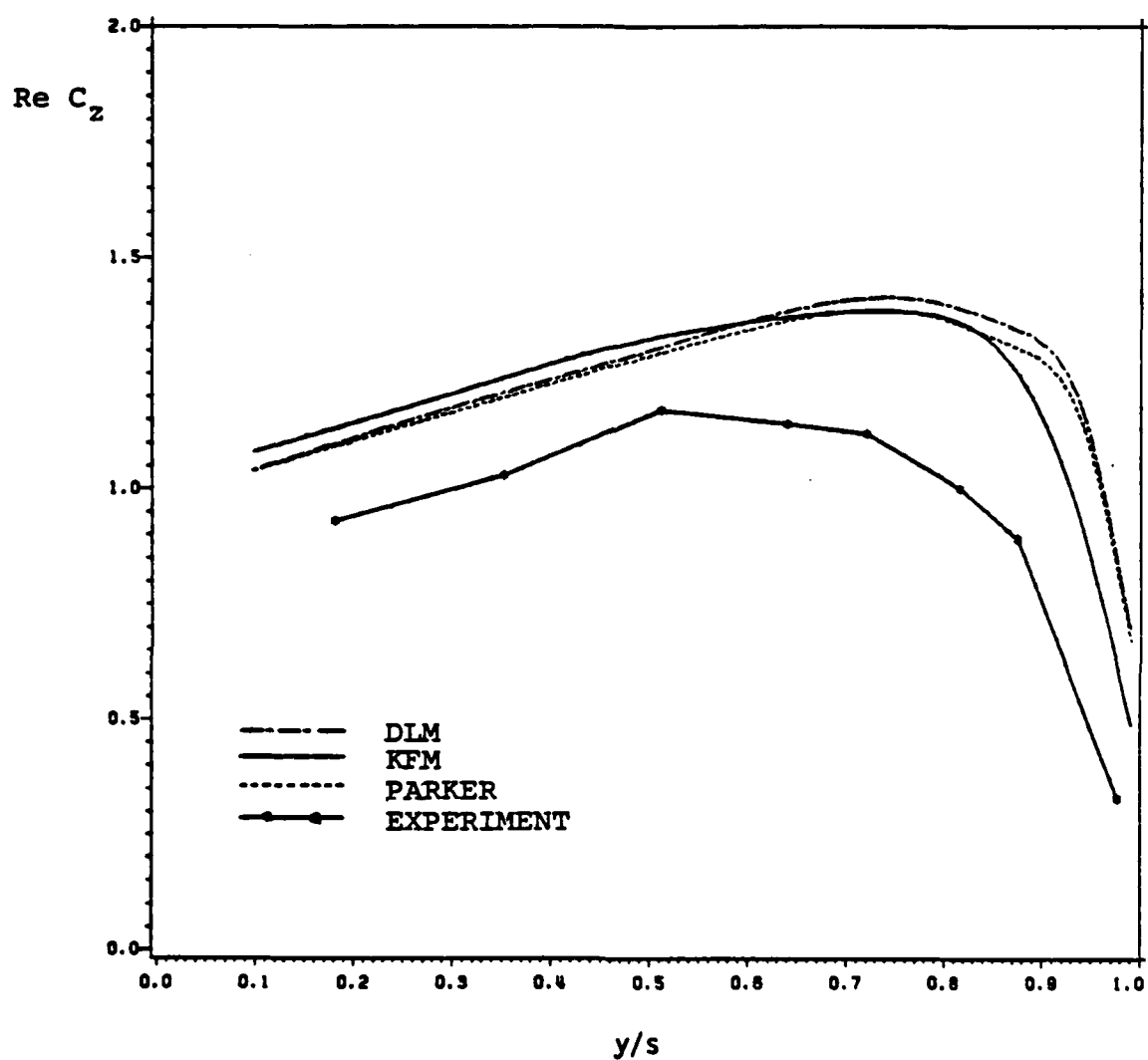


Figure 13: Unsteady Lift Coefficient Distributions of Clean Wing

Since the DLM shows only about 3% difference with Parker's results, this code seems promising. And even though the difference between the results from the kernel function code and from Parker is somewhat larger, the ANKF code shows still good enough comparison to be used for the analysis since its distribution is closer to the experimental results near the wing tip.

#### 4.2 DOUBLET LATTICE METHOD

The 22 models mentioned previously were investigated in the subsonic and transonic region for Mach numbers from  $M = 0.6 - 0.9$  by use of the doublet lattice method code (H7WC). Plots of the unsteady lift coefficient distributions are shown in Figures 14 through 17 for the wing with the missile modeled by different combinations of plates, by an octagonal cylinder, and by a cylindrical slender body.

As shown in the figures, the results of the DLM present higher distributions than the experimental results. Compared to the clean wing, the missile increases the loads over the entire wing with a greater effect in the tip region. As can be seen, the lift coefficient distributions of the endplate models show better comparison with the experimental result in the tip region. Model 2, where the middle of the endplate is positioned next to the launcher, reveals very good agreement with model 19, where the endplate is located above the outer launcher edge.

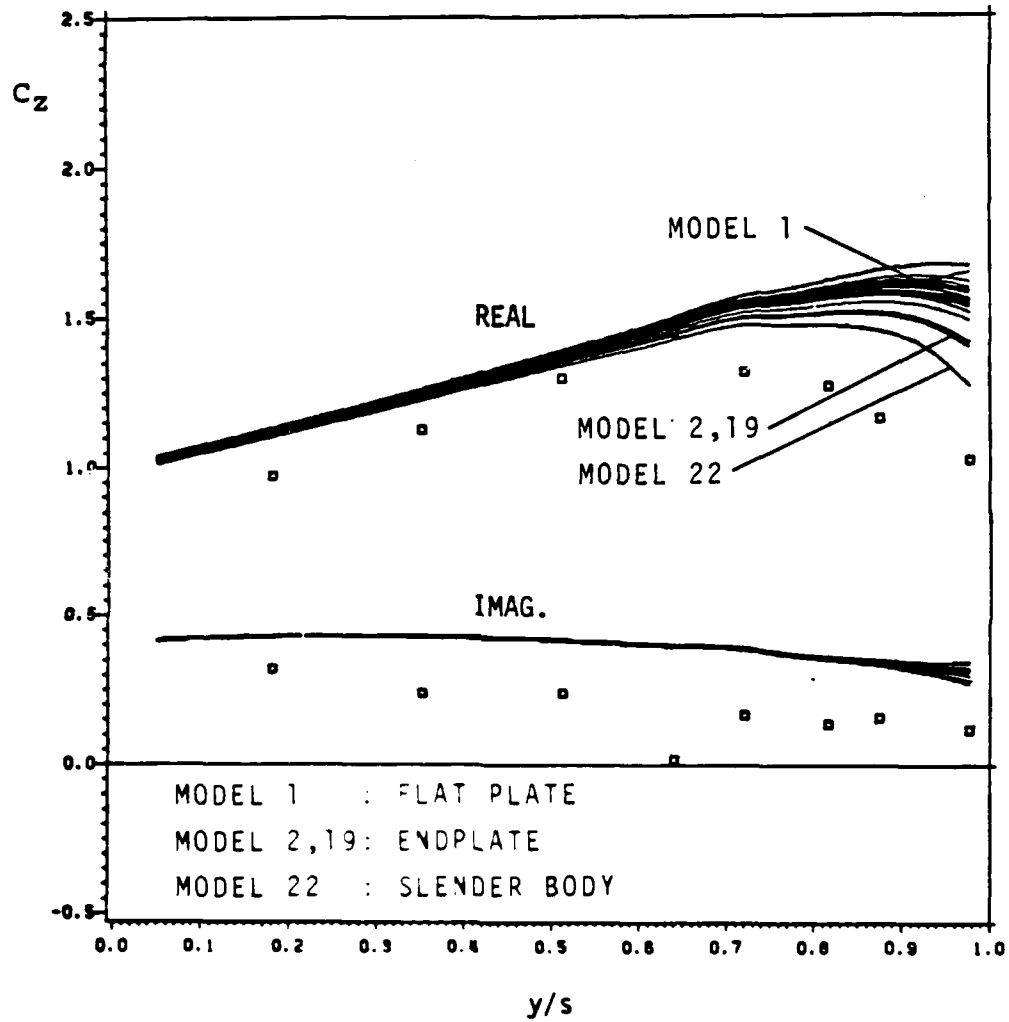


Figure 14: Unsteady Lift Coefficient Distributions ( $M=0.6$ ,  $k=0.200$ , DLM, 22 Models)



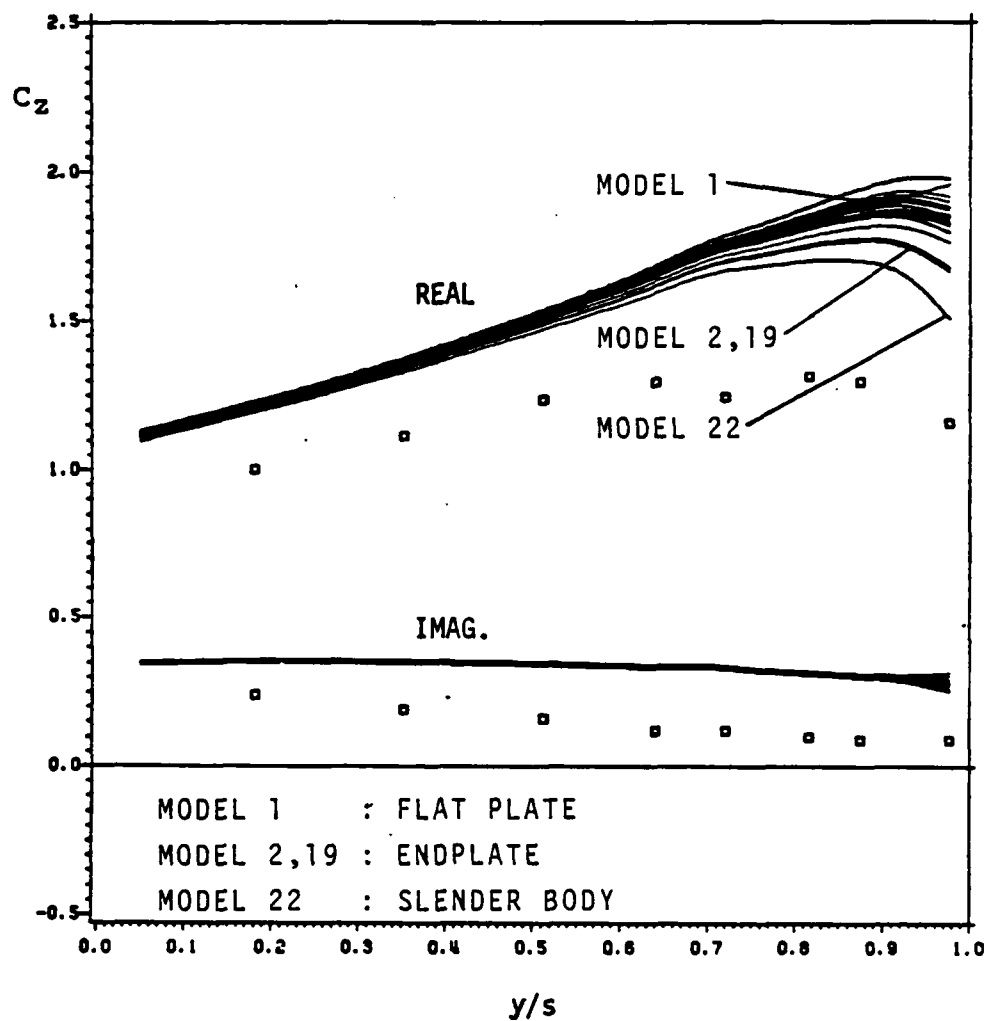


Figure 15: Unsteady Lift Coefficient Distributions ( $M=0.7$ ,  $k=0.173$ , DLM, 22 Models)

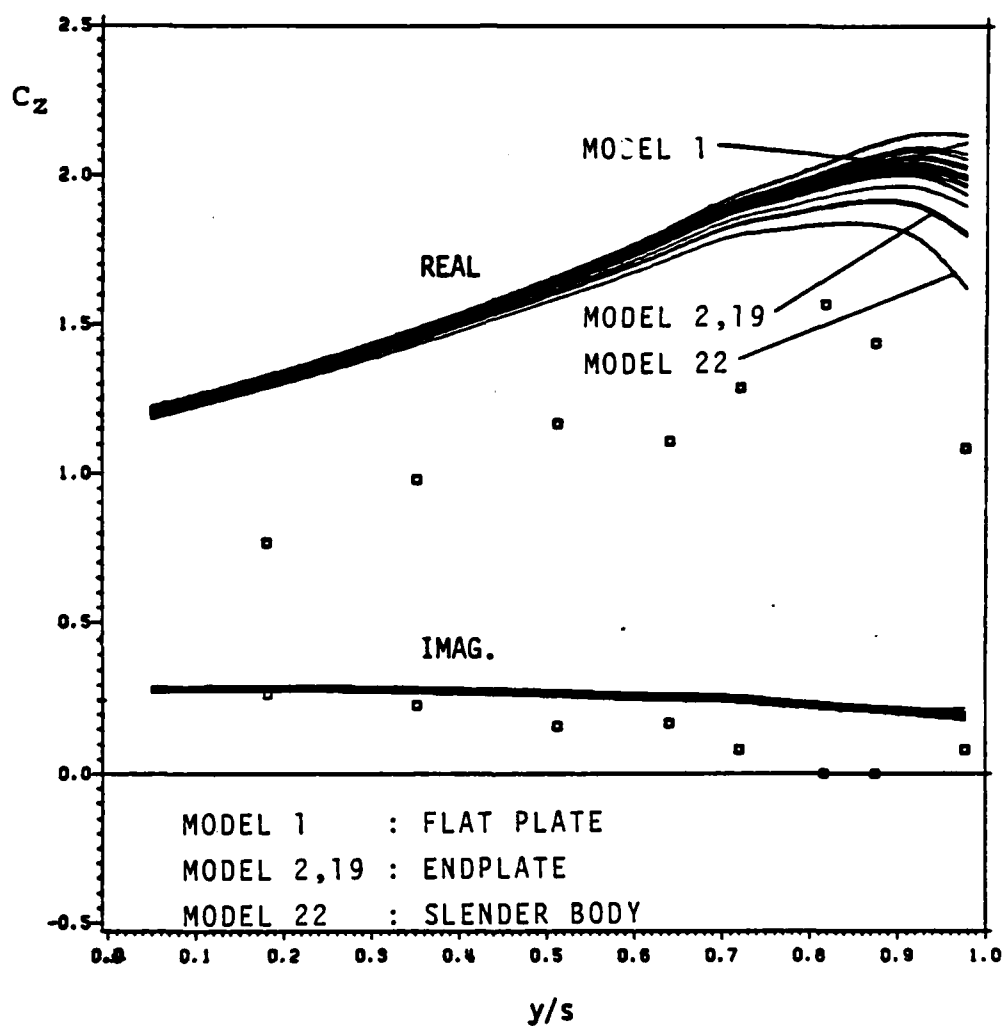


Figure 16: Unsteady Lift Coefficient Distributions ( $M=0.8$ ,  $k=0.153$ , DLM, 22 Models)

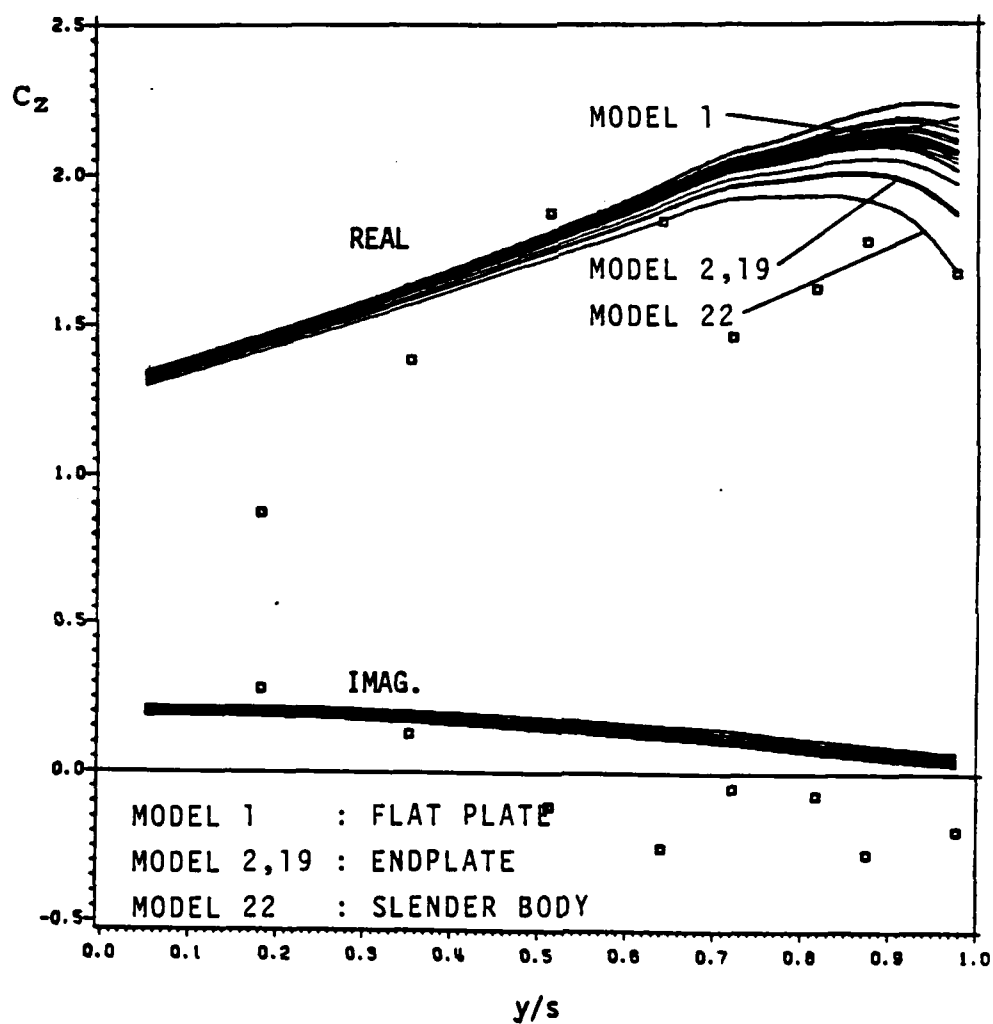


Figure 17: Unsteady Lift Coefficient Distributions ( $M=0.9$ ,  $k=0.138$ , DLM, 22 Models)

Another endplate model, model 20, where the endplate lies underneath the outer launcher edge, shows a higher lift distribution in the tip region. Model 1, in which the missile was modeled by a flat plate, and model 18, where the missile was modeled by three plates at 120 degrees to each other, show distributions similar to each other. As stated earlier, the flat plate model is widely used at present to model external bodies or stores.

The cylindrical slender body, model 22, shows the lowest loads in the tip region. The other models such as the combinations of flat plates and endplates, the octagonal cylinder, and the cruciform model presented increased loads in the tip region. The loads distribution for these models can hardly be differentiated. Therefore, to compare the models in more detail, 8 representative models were picked out of the previous 22.

1. Flat plate (Model 1)
- 2-4. Endplate - 3 different types (Models 2, 19, and 20)
5. Combination of flat plate and endplate (Model 4)
6. Cruciform (Model 14)
7. Octagonal cylinder (Model 21)
8. Slender body cylinder (Model 22)

The unsteady lift coefficient distributions of these eight models together with experimental results at  $M=0.6$  are presented in Tables 3 and 4 and in Figure 18.

TABLE 3

Unsteady Lift Coefficient Distributions (Real,  $M=0.6$ ,  
 $k=0.200$ , DLM, 8 Models)

Wing Section	1	2	3	4	5	6	7	8
Model 1	1.12	1.24	1.36	1.46	1.52	1.55	1.57	1.51
Model 2	1.11	1.23	1.35	1.44	1.49	1.51	1.51	1.40
Model 4	1.12	1.25	1.38	1.48	1.55	1.59	1.62	1.61
Model 14	1.12	1.25	1.37	1.47	1.54	1.57	1.59	1.55
Model 19	1.11	1.23	1.34	1.44	1.49	1.50	1.50	1.39
Model 20	1.11	1.23	1.35	1.45	1.51	1.53	1.54	1.48
Model 21	1.12	1.24	1.36	1.46	1.53	1.56	1.58	1.53
Model 22	1.10	1.22	1.33	1.42	1.47	1.46	1.44	1.26
EXP	0.97	1.12	1.29	1.44	1.31	1.26	1.15	1.01

TABLE 4

Unsteady Lift Coefficient Distributions (Imag,  $M=0.6$ ,  
 $k=0.200$ , DLM, 8 Models)

Wing Section	1	2	3	4	5	6	7	8
Model 1	0.43	0.43	0.42	0.40	0.39	0.36	0.35	0.31
Model 2	0.43	0.43	0.42	0.40	0.39	0.36	0.34	0.30
Model 4	0.43	0.43	0.42	0.40	0.39	0.36	0.35	0.33
Model 14	0.43	0.43	0.42	0.40	0.39	0.36	0.35	0.32
Model 19	0.43	0.43	0.42	0.40	0.39	0.36	0.34	0.29
Model 20	0.43	0.43	0.42	0.40	0.40	0.36	0.35	0.32
Model 21	0.43	0.43	0.42	0.40	0.39	0.36	0.34	0.30
Model 22	0.43	0.43	0.42	0.41	0.39	0.36	0.34	0.27
EXP	0.32	0.24	0.24	0.02	0.17	0.14	0.16	0.12

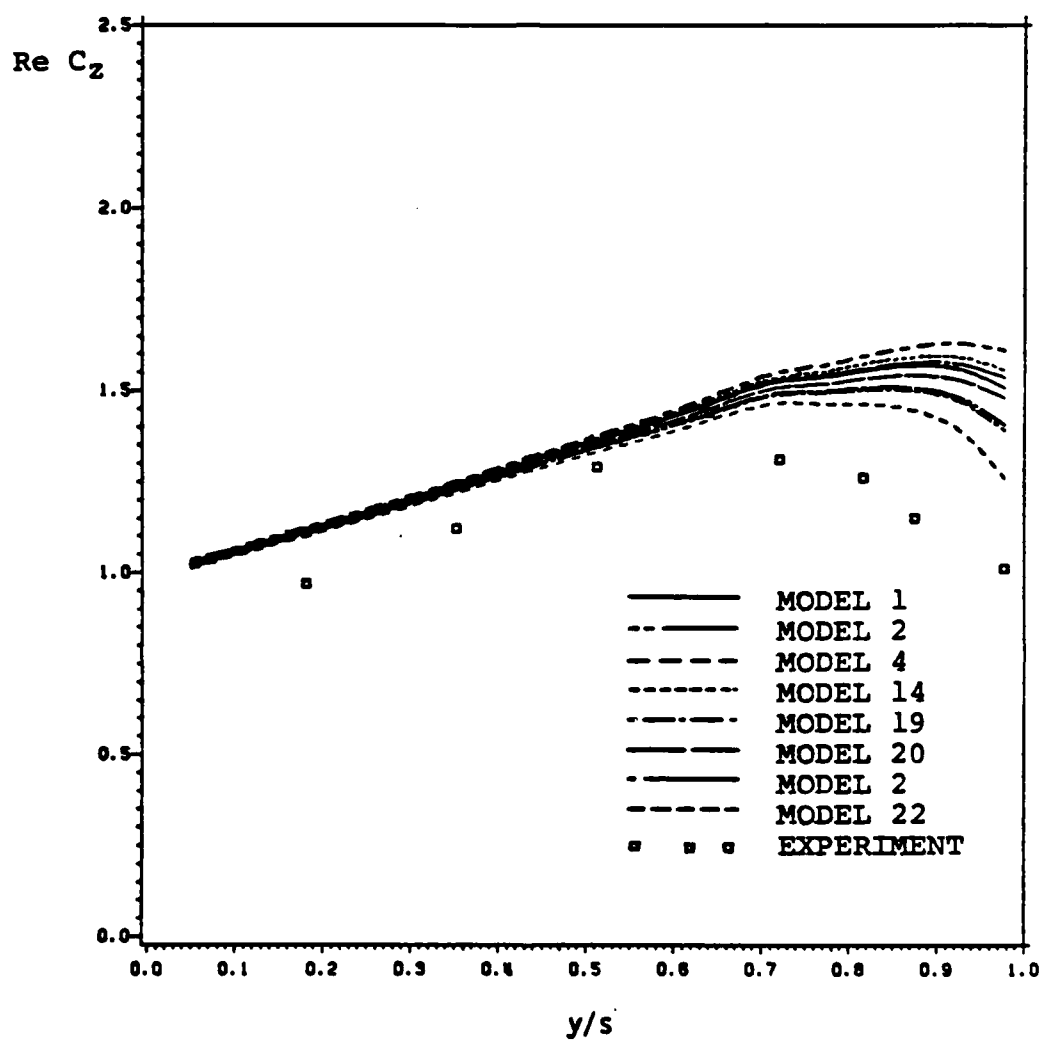


Figure 18: Unsteady Lift Coefficient Distributions ( $M=0.6$ ,  $k=0.200$ , DLM, 3 Models)

The characteristic bump present in the experimental lift distribution at about 60% semispan is barely visible in the computational results and is shifted to about 70% semispan. Overall, with the exclusion of this local increase in lift coefficient, the best computational results were those for the cylindrical slender body model and were about 10% larger than the experimental data across the wing and about 15%-20% larger in the tip region.

When the flow speed was increased to  $M=0.7$  and the reduced frequency thus lowered to  $k=0.153$ , lift was increased over the entire wing (Figure 19, Tables 5 and 6). Also, the eight models show similar distributions as for  $M=0.6$ . The differences to the experimental results, however, are increased.

As the flow speed increases to  $M=0.8$  and  $M=0.9$ , the lift coefficients of all models are increased. Results are presented in Figures 20 and 21 and in Tables 7 through 10. In these linearized transonic cases, the cylindrical slender body model shows results closest to the experimental data together with the endplate models while the cruciform and octagonal cylinder models display increased lift in the tip region. The model with the flat plate - endplate combination presents the highest lift distribution over the entire wing for every case. Since the linear code cannot predict the nonlinear transonic flow, results do not show good comparison to experimental data.

TABLE 5

Unsteady Lift Coefficient Distributions (Real,  $M=0.7$ ,  
 $k=0.173$ , DLM, 8 Models)

Wing Section	1	2	3	4	5	6	7	8
Model 1	1.21	1.35	1.51	1.65	1.74	1.81	1.84	1.79
Model 2	1.20	1.34	1.49	1.62	1.70	1.75	1.77	1.67
Model 4	1.22	1.37	1.53	1.67	1.77	1.86	1.91	1.92
Model 14	1.22	1.36	1.52	1.66	1.75	1.83	1.87	1.85
Model 19	1.20	1.34	1.48	1.61	1.70	1.75	1.76	1.66
Model 20	1.21	1.35	1.50	1.63	1.72	1.78	1.81	1.76
Model 21	1.21	1.36	1.51	1.65	1.74	1.82	1.86	1.83
Model 22	1.19	1.33	1.47	1.59	1.67	1.70	1.70	1.50
EXP	1.00	1.11	1.23	1.29	1.24	1.31	1.29	1.15

TABLE 6

Unsteady Lift Coefficient Distributions (Imag,  $M=0.7$ ,  
 $k=0.173$ , DLM, 8 Models)

Wing Section	1	2	3	4	5	6	7	8
Model 1	0.35	0.35	0.34	0.34	0.33	0.32	0.31	0.28
Model 2	0.36	0.35	0.35	0.34	0.34	0.32	0.31	0.27
Model 4	0.35	0.35	0.34	0.33	0.33	0.31	0.31	0.29
Model 14	0.35	0.35	0.34	0.34	0.33	0.32	0.31	0.29
Model 19	0.36	0.35	0.35	0.34	0.33	0.31	0.30	0.26
Model 20	0.36	0.35	0.35	0.34	0.34	0.32	0.31	0.29
Model 21	0.35	0.35	0.34	0.33	0.33	0.31	0.30	0.27
Model 22	0.36	0.36	0.35	0.34	0.34	0.32	0.30	0.25
EXP	0.24	0.19	0.16	0.12	0.12	0.10	0.09	0.09



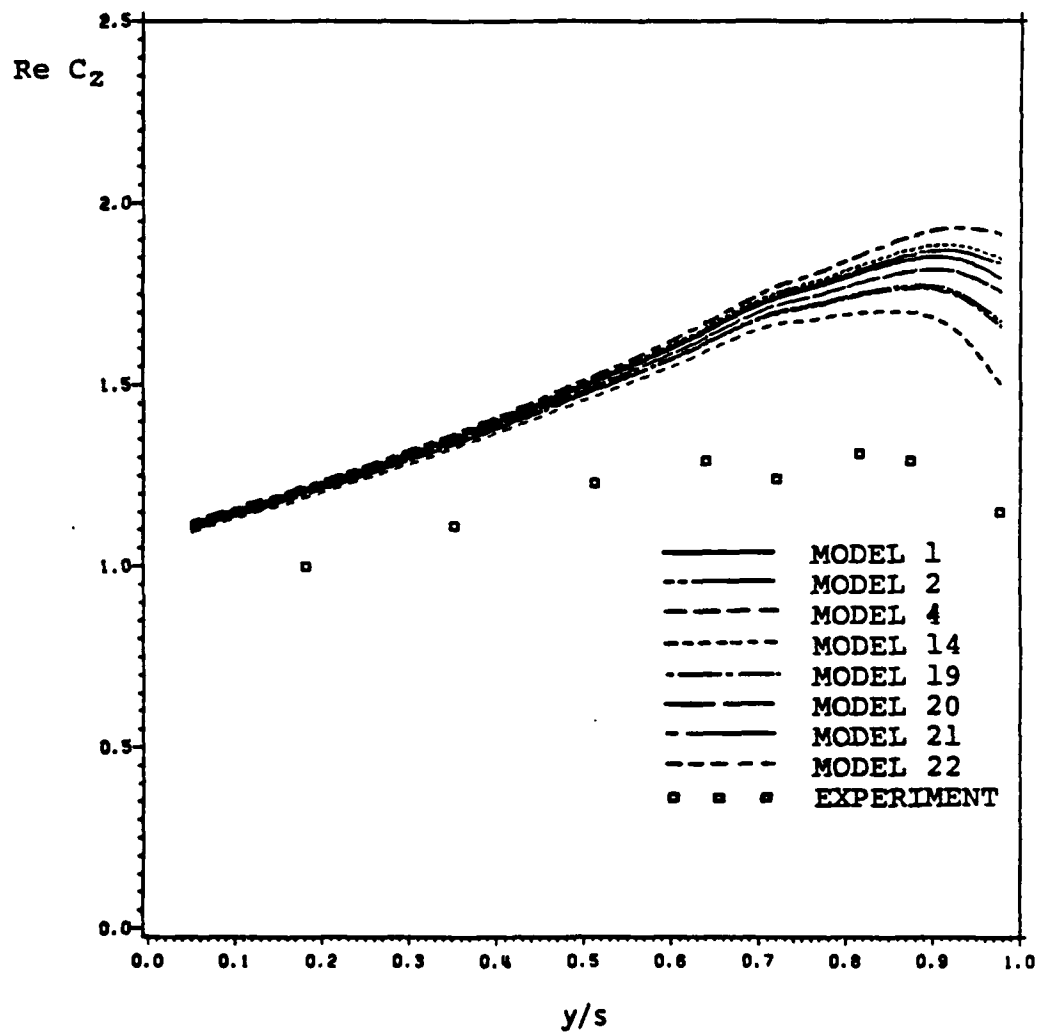


Figure 19: Unsteady Lift Coefficient Distributions ( $M=0.7$ ,  $\kappa=0.173$ , DLM, 8 Models)

TABLE 7

Unsteady Lift Coefficient Distributions (Real,  $M=0.8$ ,  
 $k=0.153$ , DLM, 8 Models)

Wing Section	1	2	3	4	5	6	7	8
Model 1	1.31	1.47	1.64	1.79	1.89	1.96	2.00	1.94
Model 2	1.30	1.45	1.61	1.75	1.84	1.90	1.92	1.81
Model 4	1.33	1.48	1.66	1.82	1.92	2.02	2.07	2.07
Model 14	1.32	1.47	1.64	1.80	1.90	1.99	2.03	1.99
Model 19	1.30	1.45	1.61	1.75	1.84	1.90	1.91	1.80
Model 20	1.30	1.46	1.62	1.77	1.86	1.93	1.96	1.90
Model 21	1.31	1.47	1.64	1.79	1.89	1.98	2.02	1.99
Model 22	1.29	1.43	1.59	1.72	1.80	1.84	1.84	1.62
EXP	0.77	0.98	1.17	1.11	1.29	1.57	1.44	1.09

TABLE 8

Unsteady Lift Coefficient Distributions (Imag,  $M=0.8$ ,  
 $k=0.153$ , DLM, 8 Models)

Wing Section	1	2	3	4	5	6	7	8
Model 1	0.29	0.28	0.27	0.25	0.25	0.23	0.22	0.19
Model 2	0.29	0.29	0.27	0.26	0.26	0.23	0.22	0.19
Model 4	0.28	0.27	0.26	0.25	0.24	0.22	0.21	0.19
Model 14	0.28	0.28	0.27	0.25	0.25	0.23	0.22	0.20
Model 19	0.29	0.29	0.27	0.26	0.25	0.23	0.22	0.18
Model 20	0.29	0.28	0.27	0.26	0.26	0.24	0.23	0.21
Model 21	0.28	0.28	0.26	0.25	0.24	0.22	0.21	0.18
Model 22	0.30	0.29	0.28	0.27	0.26	0.24	0.22	0.18
EXP	0.27	0.23	0.16	0.17	0.08	0.00	0.00	0.08

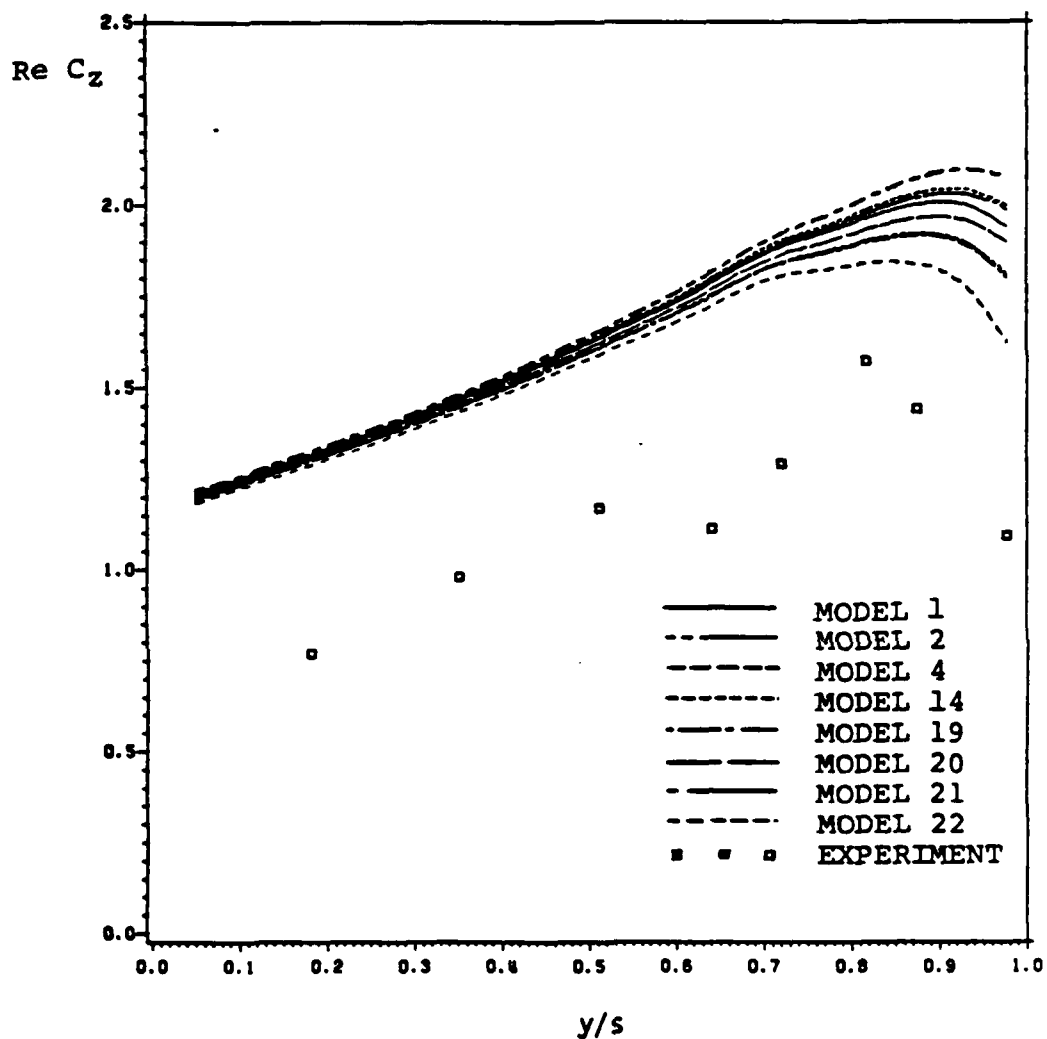


Figure 20: Unsteady Lift Coefficient Distributions ( $\gamma=0.3$ ,  $k=0.153$ , DLM, 8 Models)

TABLE 9

Unsteady Lift Coefficient Distributions (Real,  $M=0.9$ ,  
 $k=0.138$ , DLM, 8 Models)

Wing Section	1	2	3	4	5	6	7	8
Model 1	1.44	1.61	1.77	1.92	2.01	2.06	2.09	2.01
Model 2	1.43	1.58	1.74	1.88	1.96	1.99	2.00	1.86
Model 4	1.46	1.62	1.80	1.95	2.05	2.13	2.17	2.15
Model 14	1.45	1.61	1.78	1.93	2.03	2.09	2.12	2.07
Model 19	1.42	1.58	1.74	1.88	1.96	1.99	1.99	1.86
Model 20	1.43	1.59	1.76	1.90	1.98	2.03	2.04	1.96
Model 21	1.44	1.61	1.78	1.92	2.02	2.08	2.11	2.06
Model 22	1.41	1.57	1.72	1.85	1.91	1.92	1.91	1.67
EXP	0.87	1.38	1.87	1.84	1.45	1.61	1.77	1.66

TABLE 10

Unsteady Lift Coefficient Distributions (Imag,  $M=0.9$ ,  
 $k=0.138$ , DLM, 8 Models)

Wing Section	1	2	3	4	5	6	7	8
Model 1	0.20	0.18	0.16	0.13	0.12	0.09	0.07	0.05
Model 2	0.21	0.20	0.17	0.15	0.13	0.10	0.09	0.06
Model 4	0.19	0.17	0.15	0.12	0.10	0.07	0.06	0.04
Model 14	0.19	0.18	0.15	0.13	0.11	0.08	0.07	0.05
Model 19	0.21	0.19	0.17	0.15	0.13	0.10	0.08	0.05
Model 20	0.21	0.19	0.17	0.14	0.13	0.10	0.09	0.07
Model 21	0.19	0.18	0.15	0.12	0.11	0.07	0.06	0.03
Model 22	0.22	0.21	0.18	0.16	0.15	0.11	0.10	0.07
EXP	0.28	0.13	-0.11	-0.25	-0.05	-0.07	-0.27	-0.19

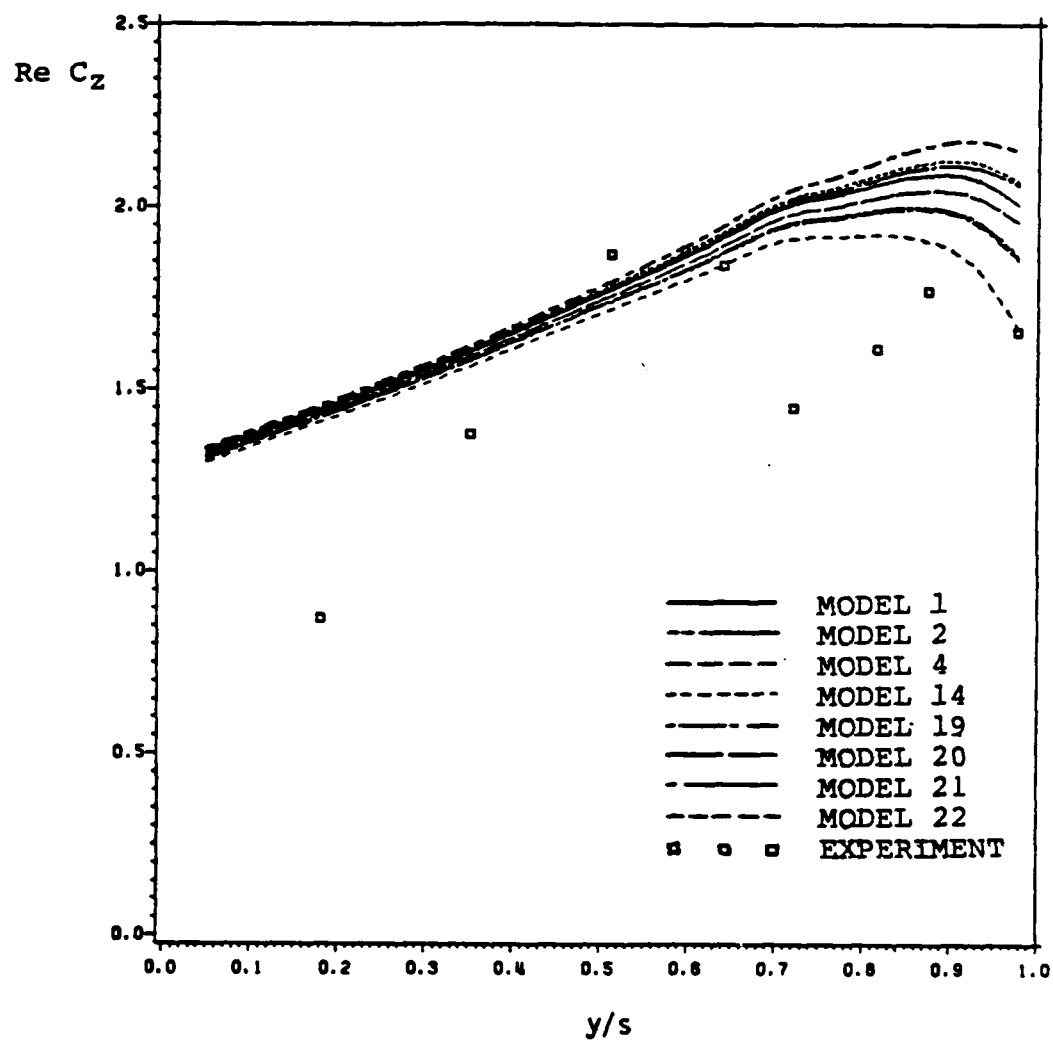


Figure 21: Unsteady Lift Coefficient Distributions ( $M=0.9$ ,  $k=0.138$ , DLM, 3 Models)

In optimizing the missile models, the effect of cost was an important factor. Thus, the amount of computer time and storage for these eight models on an IBM 3081D mainframe computer is listed in Tables 11 through 14. As can be seen in the tables, the octagonal cylinder model required the largest amount of CPU time and storage followed by the combination model and the cruciform model. The cost for the flat plate, endplate, and slender body models are less than those for the others. In addition, these models show considerably better agreement with the experimental lift distributions.

#### 4.3 KERNEL FUNCTION METHOD

In order to verify the advantage of the end-plate models, 6 models were then tested by the kernel function code. Here, the octagonal cylinder model was not used due to the highest cost and the slender body cylinder model was not tested since this type of geometry cannot be accommodated by the ANKF code.

Thus, six models were examined by use of this code as listed below:

1. Flat plate (Model 1)
- 2-4. Endplate - 3 different types (Models 2, 19, and 20)
5. Combination of flat plate and end-plate (Model 4)
6. Cruciform (Model 14)

TABLE 11

Comparison of Effort ( $M=0.6$ ,  $k=0.200$ , DLM, 8 Models)

	CPU Time (sec)	Storage I/O (K-min)	Disk I/O (EXCP)
Model 1	83.36	2338.2	6119
Model 2	88.64	2388.8	6119
Model 4	121.85	3902.3	10231
Model 14	128.87	3970.8	10231
Model 19	88.91	2391.3	6119
Model 20	91.83	2412.8	6119
Model 21	190.85	6158.9	15710
Model 22	66.04	1889.4	5081

TABLE 12

Comparison of Effort ( $M=0.7$ ,  $k=0.173$ , DLM, 8 Models)

	CPU Time (sec)	Storage I/O (K-min)	Disk I/O (EXCP)
Model 1	83.99	2345.3	6129
Model 2	89.34	2397.1	6129
Model 4	133.22	4005.0	10241
Model 14	128.60	3969.0	10241
Model 19	88.41	2388.6	6129
Model 20	88.07	2385.5	6129
Model 21	191.93	6170.6	15720
Model 22	66.03	1889.4	5081

TABLE 13

Comparison of Effort ( $M=0.8$ ,  $k=0.153$ , DLM, 8 Models)

	CPU Time (sec)	Storage I/O (K-min)	Disk I/O (EXCP)
Model 1	83.07	2337.6	6129
Model 2	87.70	2382.5	6129
Model 4	119.44	3881.8	10241
Model 14	132.22	3995.1	10241
Model 19	88.10	2386.3	6129
Model 20	87.98	2385.0	6129
Model 21	191.73	6168.9	15720
Model 22	65.86	1887.9	5081

TABLE 14

Comparison of Effort ( $M=0.9$ ,  $k=0.138$ , DLM, 8 Models)

	CPU Time (sec)	Storage I/O (K-min)	Disk I/O (EXCP)
Model 1	82.91	2336.3	6129
Model 2	87.93	2384.7	6129
Model 4	119.61	3883.6	10241
Model 14	126.84	3953.7	10241
Model 19	87.96	2384.9	6129
Model 20	87.88	2384.3	6129
Model 21	189.89	6151.9	15720
Model 22	65.58	1885.3	5081



The six models were evaluated at the same Mach numbers and reduced frequencies as in the previous section. At  $M=0.6$  and  $k=0.200$ , five of the models show lift distributions somewhat similar to those for the DLM except in the tip region where the drop in lift coefficients occurs closer toward the wing tip (Figure 22, Tables 15 and 16). Two of the endplate models, model 2 and model 19, show fairly good lift distributions compared to the experimental results while the other endplate, model 20, shows increased lift in the tip region by a significant amount. In the previous section, the flat plate model showed a higher lift distribution in the tip region than this endplate model while here this situation is reversed. The combination model, which showed the highest lift in the tip region in the DLM, presents almost the same shape for the KFM results.

It is of interest to note that the cruciform, model 14, shows highly increased lift over the entire wing surface. It seems that a singularity inherent in the matrix due to the symmetry of the model about its longitudinal axis may have caused this excessive result.

When the Mach number was increased and the reduced frequency thus decreased, lift was increased as was seen in the previous section. The lift distributions for these cases are presented in Figures 23 through 25, and in Tables 17 through 22. With the increase in Mach number, the discrepancy between the numerical and experimental results

TABLE 15

Unsteady Lift Coefficient Distributions (Real,  $M=0.6$ ,  
 $k=0.200$ , KFM, 6 Models)

Wing Span	0.0 (%)	28.2	54.1	75.6	91.0	99.0
Model 1	1.06	1.26	1.44	1.58	1.62	1.57
Model 2	1.05	1.24	1.41	1.52	1.50	1.38
Model 4	1.07	1.27	1.45	1.60	1.64	1.59
Model 14	1.24	1.50	1.85	2.39	3.29	4.27
Model 19	1.06	1.25	1.42	1.52	1.47	1.30
Model 20	1.05	1.25	1.42	1.57	1.63	1.64

TABLE 16

Unsteady Lift Coefficient Distributions (Imag,  $M=0.6$ ,  
 $k=0.200$ , KFM, 6 Models)

Wing Span	0.0 (%)	28.2	54.1	75.6	91.0	99.0
Model 1	0.31	0.31	0.31	0.31	0.31	0.31
Model 2	0.31	0.31	0.31	0.31	0.31	0.31
Model 4	0.31	0.31	0.31	0.31	0.31	0.31
Model 14	0.28	0.28	0.28	0.28	0.28	0.28
Model 19	0.34	0.34	0.34	0.34	0.34	0.34
Model 20	0.28	0.28	0.28	0.28	0.28	0.28

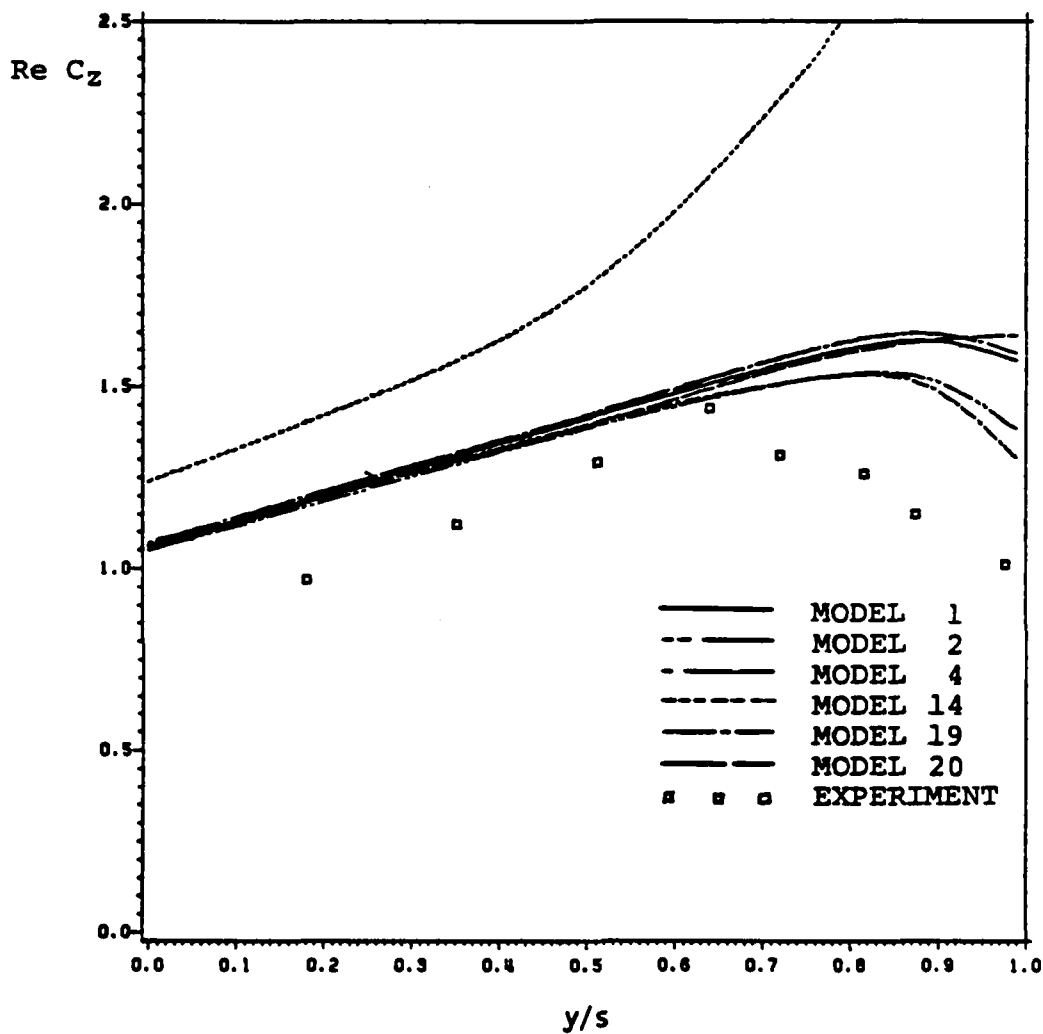


Figure 22: Unsteady Lift Coefficient Distributions ( $M=0.6$ ,  $k=0.200$ , KF1, 6 Models)

TABLE 17

Unsteady Lift Coefficient Distributions (Real,  $M=0.7$ ,  
 $k=0.173$ , KFM, 6 Models)

Wing Span	0.0 (%)	28.2	54.1	75.6	91.0	99.0
Model 1	1.13	1.34	1.54	1.71	1.77	1.72
Model 2	1.12	1.32	1.51	1.65	1.63	1.51
Model 4	1.14	1.35	1.55	1.73	1.79	1.74
Model 14	1.37	1.67	2.08	2.74	3.79	4.90
Model 19	1.13	1.34	1.52	1.65	1.60	1.43
Model 20	1.11	1.32	1.52	1.69	1.78	1.79

TABLE 18

Unsteady Lift Coefficient Distributions (Imag,  $M=0.7$ ,  
 $k=0.173$ , KFM, 6 Models)

Wing Span	0.0 (%)	28.2	54.1	75.6	91.0	99.0
Model 1	0.25	0.25	0.25	0.25	0.25	0.25
Model 2	0.25	0.25	0.25	0.25	0.25	0.25
Model 4	0.25	0.25	0.25	0.25	0.25	0.25
Model 14	0.20	0.20	0.20	0.20	0.20	0.20
Model 19	0.30	0.30	0.30	0.30	0.30	0.30
Model 20	0.21	0.21	0.21	0.21	0.21	0.21

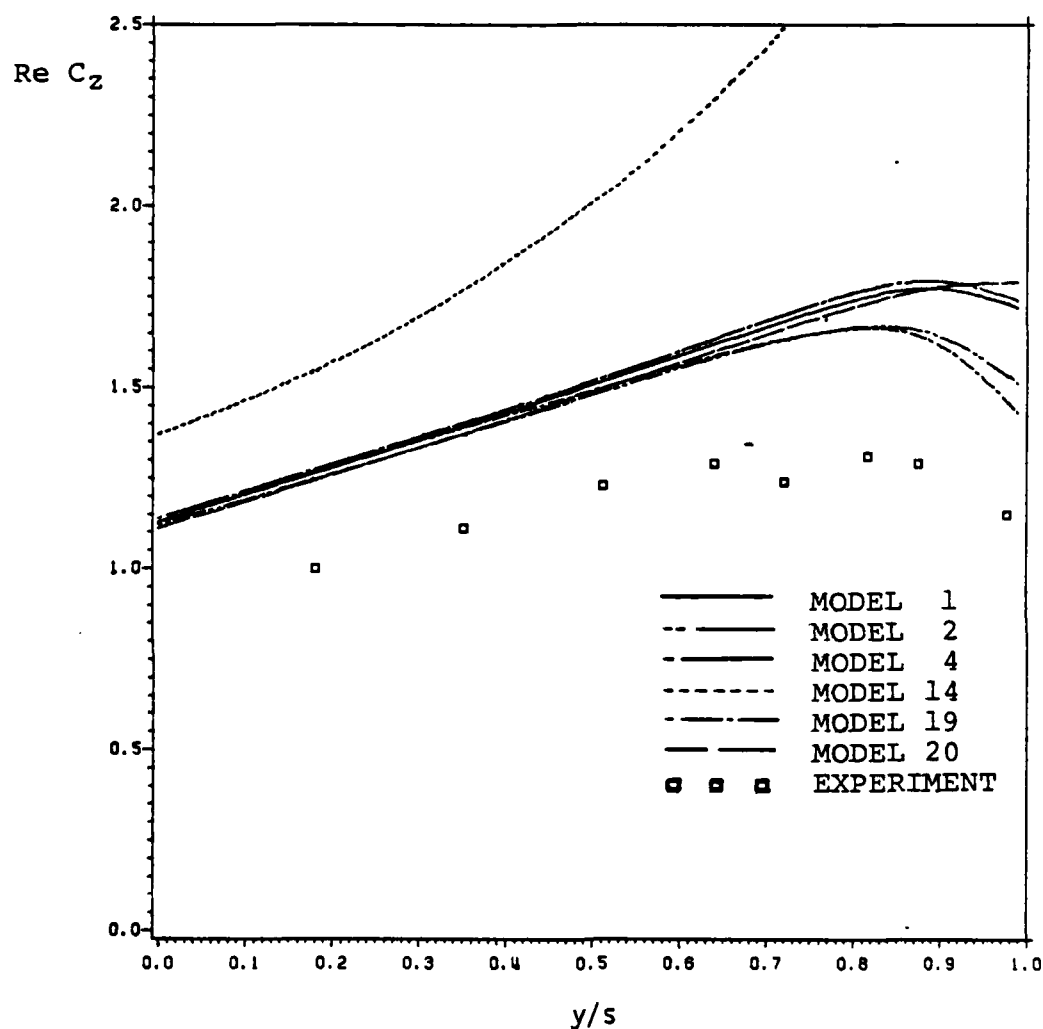


Figure 23: Unsteady Lift Coefficient Distributions ( $M=0.7$ ,  $k=0.173$ , KFM, 6 Models)

TABLE 19

Unsteady Lift Coefficient Distributions (Real,  $M=0.8$ ,  
 $k=0.153$ , KFM, 6 Models)

Wing Span	0.0 (%)	28.2	54.1	75.6	91.0	99.0
Model 1	1.23	1.46	1.68	1.87	1.92	1.86
Model 2	1.21	1.44	1.64	1.79	1.77	1.62
Model 4	1.24	1.48	1.70	1.89	1.94	1.86
Model 14	1.53	1.87	2.33	3.04	4.12	5.23
Model 19	1.22	1.46	1.66	1.80	1.76	1.57
Model 20	1.21	1.44	1.65	1.83	1.91	1.89

TABLE 20

Unsteady Lift Coefficient Distributions (Imag,  $M=0.8$ ,  
 $k=0.153$ , KFM, 6 Models)

Wing Span	0.0 (%)	28.2	54.1	75.6	91.0	99.0
Model 1	0.20	0.20	0.20	0.20	0.20	0.20
Model 2	0.21	0.21	0.21	0.21	0.21	0.21
Model 4	0.20	0.20	0.20	0.20	0.20	0.20
Model 14	0.13	0.13	0.13	0.13	0.13	0.13
Model 19	0.26	0.26	0.26	0.26	0.26	0.26
Model 20	0.15	0.15	0.15	0.15	0.15	0.15

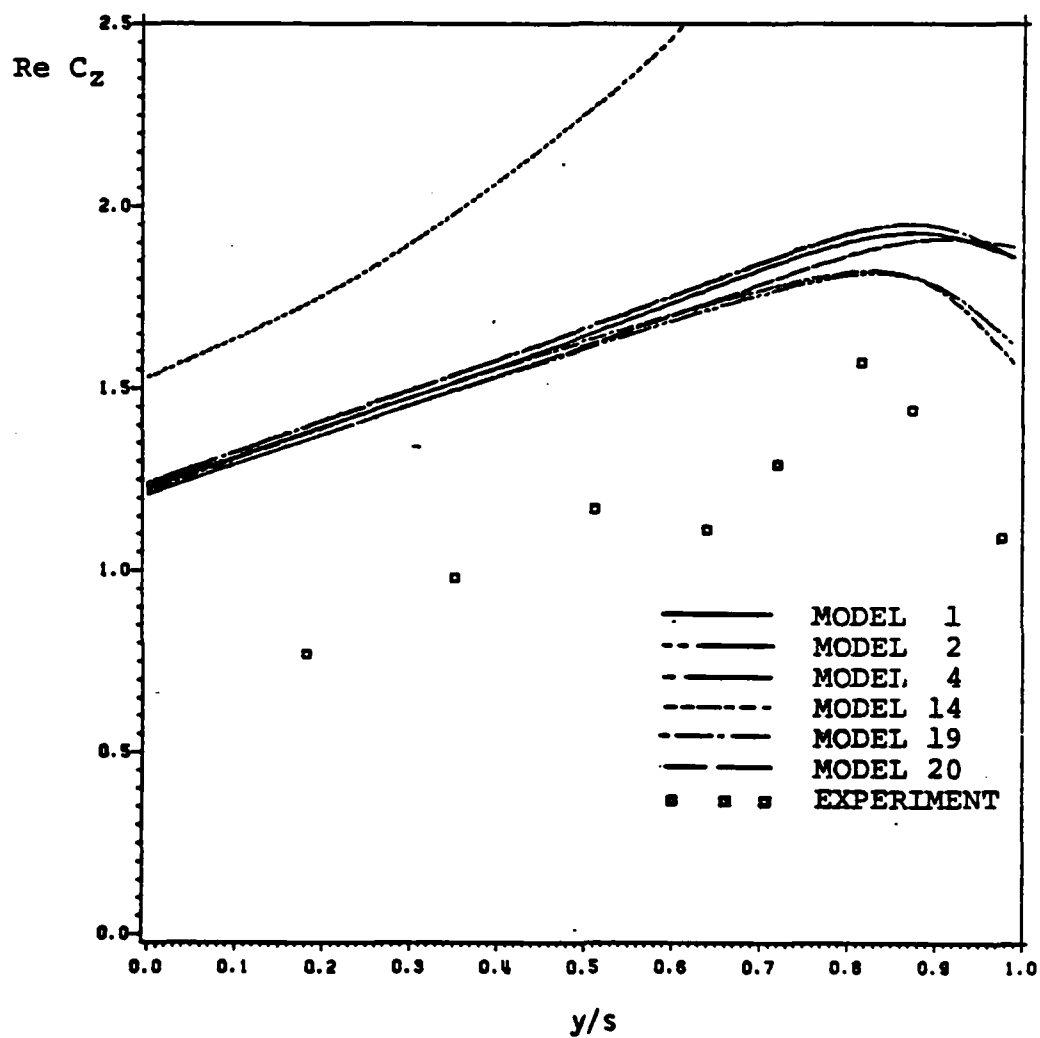


Figure 24: Unsteady Lift Coefficient Distributions ( $M=0.8$ ,  $k=0.153$ , KFM, 6 Models)

TABLE 21

Unsteady Lift Coefficient Distributions (Real,  $M=0.9$ ,  
 $k=0.138$ , KFM, 6 Models)

Wing Span	0.0 (%)	28.2	54.1	75.6	91.0	99.0
Model 1	1.39	1.67	1.92	2.11	2.15	2.06
Model 2	1.37	1.63	1.86	2.01	1.97	1.79
Model 4	1.43	1.71	1.97	2.16	2.18	2.06
Model 14	1.86	2.27	2.84	3.65	4.82	5.98
Model 19	1.40	1.66	1.90	2.04	1.97	1.75
Model 20	1.36	1.62	1.87	2.05	2.11	2.08

TABLE 22

Unsteady Lift Coefficient Distributions (Imag,  $M=0.9$ ,  
 $k=0.138$ , KFM, 6 Models)

Wing Span	0.0 (%)	28.2	54.1	75.6	91.0	99.0
Model 1	0.14	0.14	0.14	0.14	0.14	0.14
Model 2	0.15	0.15	0.15	0.15	0.15	0.15
Model 4	0.14	0.14	0.14	0.14	0.14	0.14
Model 14	0.01	0.01	0.01	0.01	0.01	0.01
Model 19	0.23	0.23	0.23	0.23	0.23	0.23
Model 20	0.06	0.06	0.06	0.06	0.06	0.06



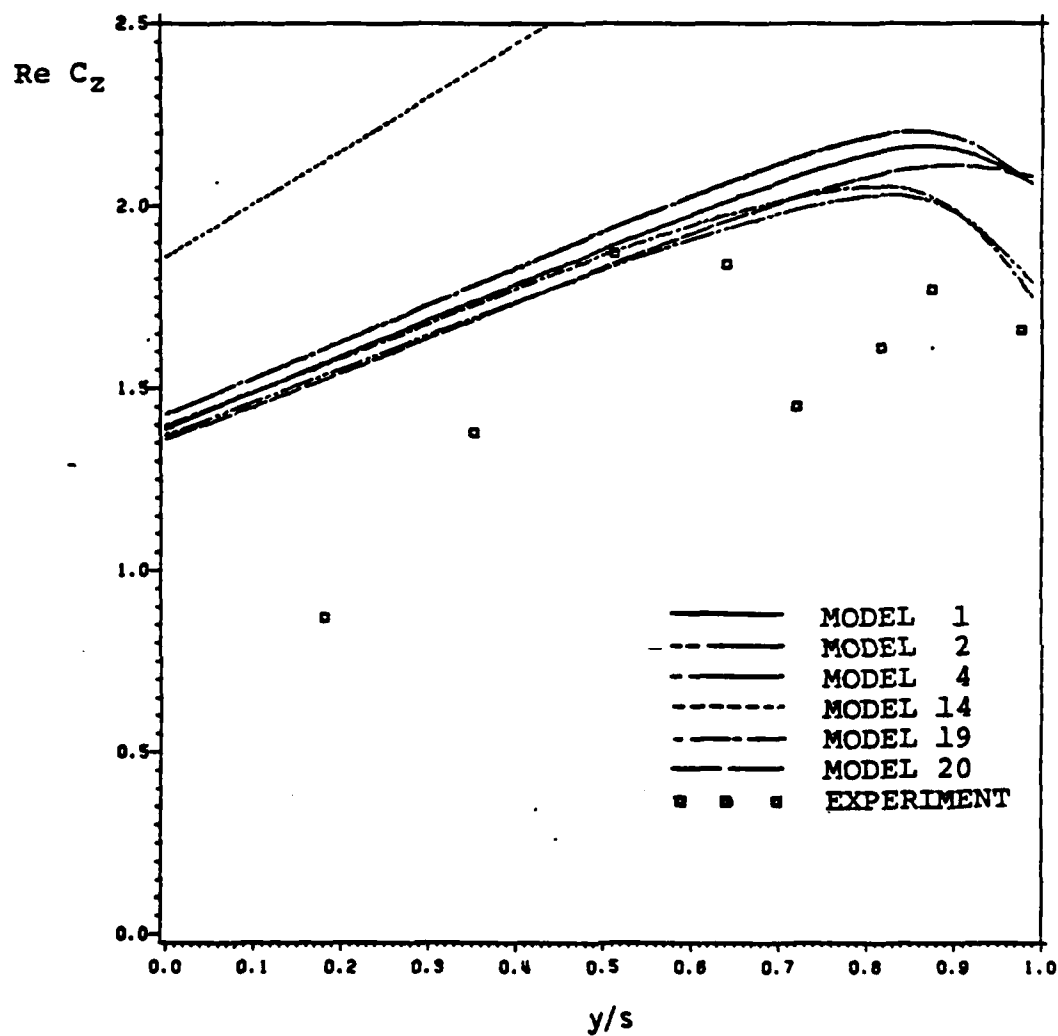


Figure 25: Unsteady Lift Coefficient Distributions ( $M=0.9$ ,  $k=0.138$ , KFM, 6 Models)

for the lift from the mid-section to the tip-section was broadened. As for the two best models, the lift distribution of model 19 grew just very little faster than that of model 2. It also shows a slightly larger value in the tip region than for the DLM.

Again, the bumps in the transonic experimental pressure distributions were not modeled by the numerics. Also, the discrepancies between the experimental and the numerical results increased with increased Mach number and decreased reduced frequency due to the linearity of the code, since the numerical results do not reflect shock waves possibly present in the transonic cases  $M=0.8$  and  $0.9$ .

The six models were also analyzed in the supersonic region. The lift coefficient distributions are given in Figures 26 and 27, and in Tables 23 through 26 .

At  $M=1.1$ , model 20 shows the lowest lift from root to the 80% span station but shows a significant increase in lift in the tip region. Model 2 exhibits an almost linear distribution along the span and has less lift in the tip region than any other model. Model 19, which showed reasonably good distributions in the subsonic cases experiences more lift than the other endplate models. The flat plate model shows less lift from the root-section to the mid-section of the wing but abruptly increased lift in the tip region. The cruciform model and the combination model show high lift distributions over the entire wing.

TABLE 23

Unsteady Lift Coefficient Distributions (Real,  $M=1.1$ ,  
 $k=0.116$ , KFM, 6 Models)

Wing Span	0.0 (%)	28.2	54.1	75.6	91.0	99.0
Model 1	1.27	1.52	1.76	1.99	2.19	2.38
Model 2	1.26	1.50	1.73	1.92	2.04	2.13
Model 4	1.33	1.59	1.85	2.10	2.34	2.57
Model 14	1.65	2.07	2.74	3.77	5.58	7.73
Model 19	1.32	1.57	1.80	1.98	2.09	2.16
Model 20	1.20	1.45	1.69	1.91	2.12	2.33

TABLE 24

Unsteady Lift Coefficient Distributions (Imag,  $M=1.1$ ,  
 $k=0.116$ , KFM, 6 Models)

Wing Span	0.0 (%)	28.2	54.1	75.6	91.0	99.0
Model 1	0.29	0.29	0.29	0.29	0.29	0.29
Model 2	0.28	0.28	0.28	0.28	0.28	0.28
Model 4	0.31	0.31	0.31	0.31	0.31	0.31
Model 14	0.55	0.55	0.55	0.55	0.55	0.55
Model 19	0.22	0.22	0.22	0.22	0.22	0.22
Model 20	0.35	0.35	0.35	0.35	0.35	0.35

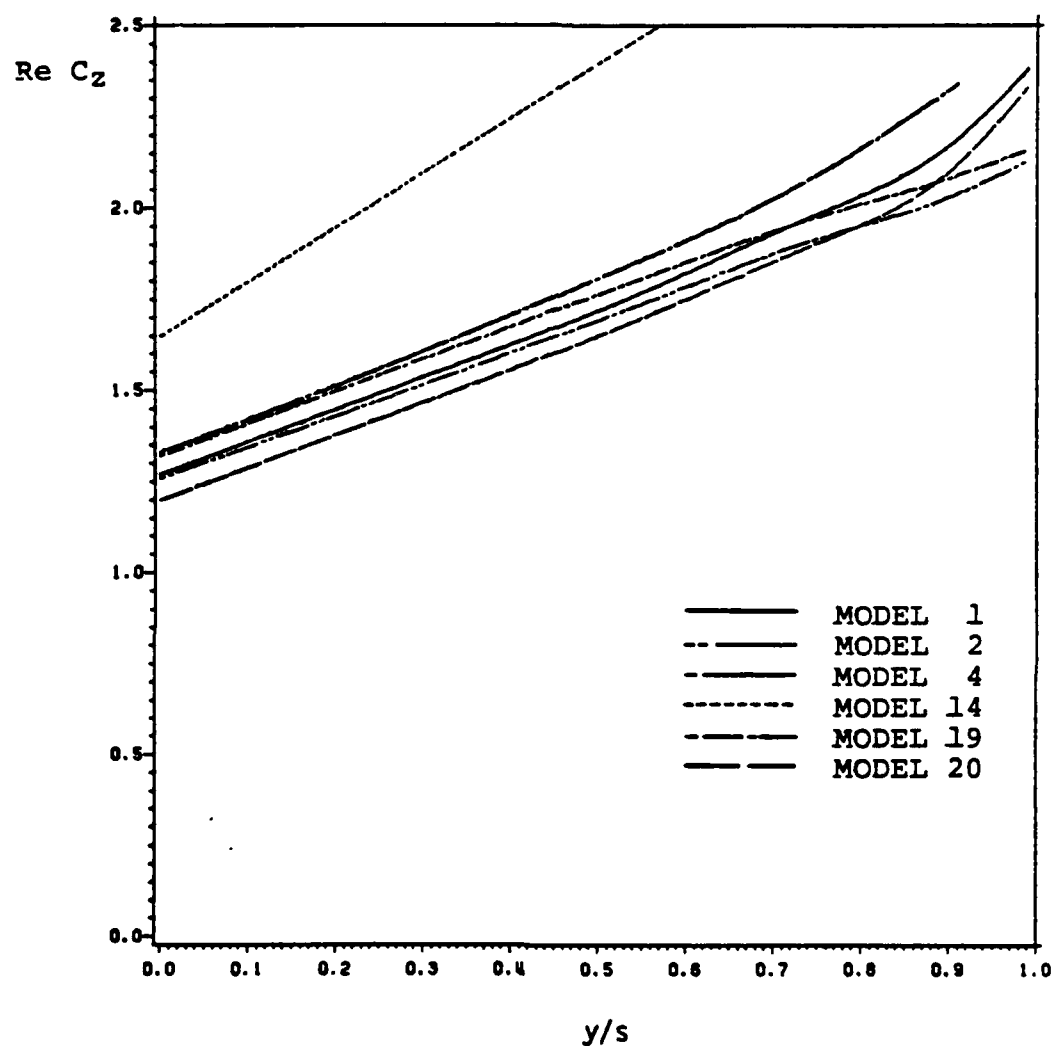


Figure 26: Unsteady Lift Coefficient Distributions ( $M=1.1$ ,  $k=0.116$ , KFM, 6 Models)

TABLE 25

Unsteady Lift Coefficient Distributions (Real,  $M=1.35$ ,  
 $k=0.101$ , KFM, 6 Models)

Wing Span	0.0 (%)	28.2	54.1	75.6	91.0	99.0
Model 1	1.02	1.19	1.41	1.70	1.94	2.19
Model 2	1.02	1.19	1.40	1.65	1.82	1.98
Model 4	1.03	1.21	1.44	1.75	2.04	2.32
Model 14	1.04	1.18	1.50	2.33	3.76	5.47
Model 19	1.02	1.19	1.41	1.67	1.85	2.01
Model 20	1.02	1.19	1.40	1.67	1.89	2.13

TABLE 26

Unsteady Lift Coefficient Distributions (Imag,  $M=1.35$ ,  
 $k=0.101$ , KFM, 6 Models)

Wing Span	0.0 (%)	28.2	54.1	75.6	91.0	99.0
Model 1	0.06	0.06	0.06	0.06	0.06	0.06
Model 2	0.06	0.06	0.06	0.06	0.06	0.06
Model 4	0.06	0.06	0.06	0.06	0.06	0.06
Model 14	0.07	0.07	0.07	0.07	0.07	0.07
Model 19	0.06	0.06	0.06	0.06	0.06	0.06
Model 20	0.06	0.06	0.06	0.06	0.06	0.06

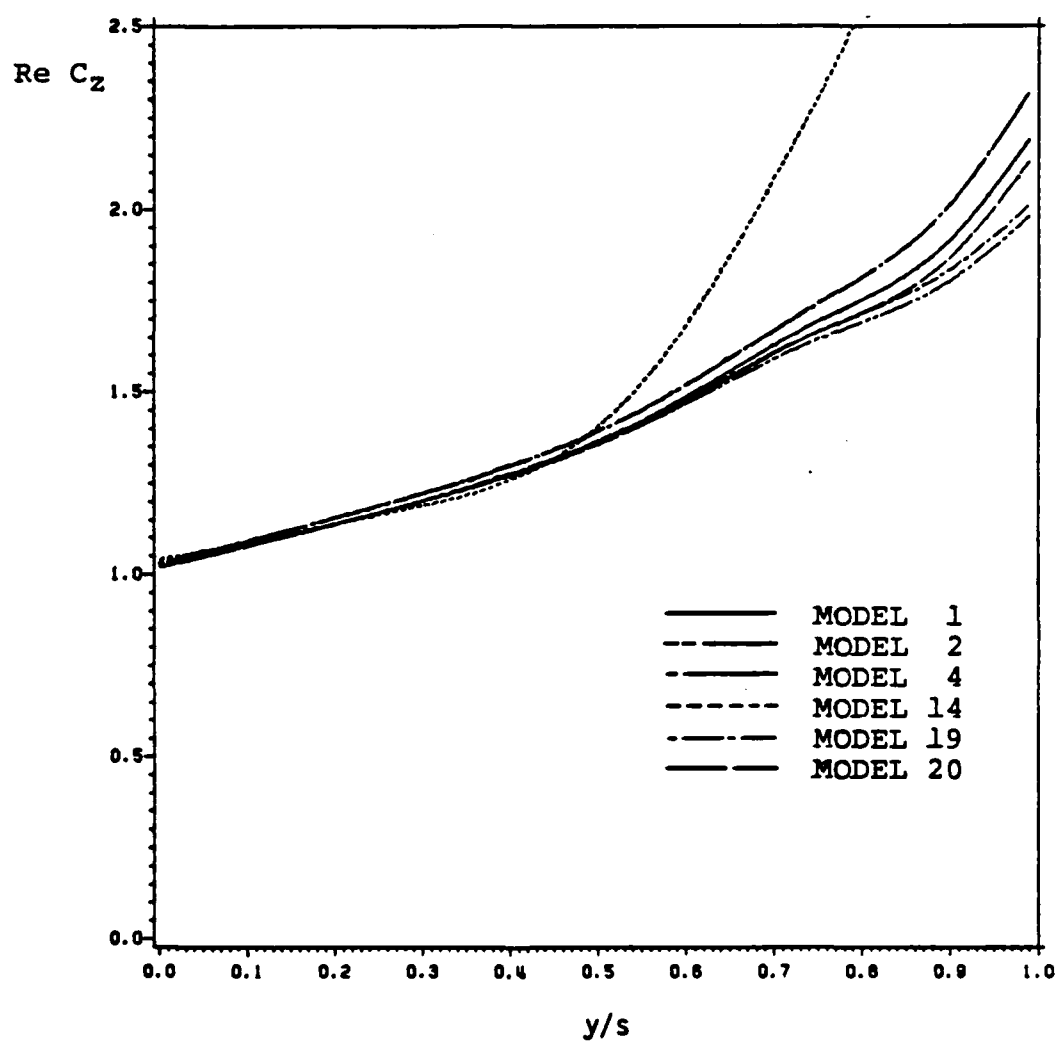


Figure 27: Unsteady Lift Coefficient Distributions ( $M=1.35$ ,  $k=0.101$ , KFM, 6 Models)

When the flow became more supersonic,  $M=1.35$ , the lift distributions of all six models dropped by a considerable amount (20% at the root). Otherwise, they showed almost the same distributions from the root section to the mid-section and slightly increased lift in the tip region. The cruciform still shows an abrupt increase starting at the mid-section. The endplate models, again, gave lower lift distributions than the other models. No experimental results were available for comparison.

The computational efforts for these models by the KFM are listed in Tables 27 through 32. As can be seen, the KFM is faster than the DLM and needs less storage. And as in the DLM, the endplate models take less computer time and storage than the other models.

#### 4.4 COMPARISON

From sections 4.2 and 4.3, we can deduce the superiority of the cylindrical slender body model and the endplate models over the other models. Therefore, in this section, a comparison was conducted of the endplate models 2 and 19, the slender body model 22, and the flat plate model 1 with the results of Dusto's complete model (8) and with the experimental results of NLR (9).

Here, the unsteady pressure distributions in chordwise direction were compared at  $M=0.8$  for sections 2, 5, and 8. These pressures are listed in Tables 33 through 38 and shown in Figures 28 through 33.

TABLE 27

Comparison of Effort ( $M=0.6$ ,  $k=0.200$ , KFM, 6 Models)

	CPU Time (sec)	Storage I/O (K-min)	Disk I/O (EXCP)
Model 1	37.27	647.5	1716
Model 2	38.46	687.1	1812
Model 4	37.30	647.9	1716
Model 14	40.96	780.2	2051
Model 19	37.92	653.3	1715
Model 20	37.60	650.4	1715

TABLE 28

Comparison of Effort ( $M=0.7$ ,  $k=0.173$ , KFM, 6 Models)

	CPU Time (sec)	Storage I/O (K-min)	Disk I/O (EXCP)
Model 1	37.24	649.7	1729
Model 2	38.32	688.5	1825
Model 4	37.21	649.7	1729
Model 14	40.78	782.2	2064
Model 19	37.44	651.3	1728
Model 20	37.39	650.8	1728



TABLE 29

Comparison of Effort ( $M=0.8$ ,  $k=0.153$ , KFM, 6 Models)

	CPU Time (sec)	Storage I/O (K-min)	Disk I/O (EXCP)
Model 1	37.21	649.5	1729
Model 2	38.15	686.7	1825
Model 4	37.08	648.2	1729
Model 14	40.24	776.9	2064
Model 19	37.59	652.7	1728
Model 20	37.29	650.0	1728

TABLE 30

Comparison of Effort ( $M=0.9$ ,  $k=0.138$ , KFM, 6 Models)

	CPU Time (sec)	Storage I/O (K-min)	Disk I/O (EXCP)
Model 1	37.56	652.4	1729
Model 2	38.22	687.3	1825
Model 4	37.75	654.1	1729
Model 14	40.75	781.6	2064
Model 19	37.69	653.6	1728
Model 20	37.71	653.7	1728

TABLE 31

Comparison of Effort ( $M=1.10$ ,  $k=0.116$ , KFM, 6 Models)

	CPU Time (sec)	Storage I/O (K-min)	Disk I/O (EXCP)
Model 1	38.55	662.3	1729
Model 2	41.64	720.2	1825
Model 4	38.77	664.3	1729
Model 14	47.23	844.5	2064
Model 19	39.47	670.8	1728
Model 20	39.47	670.9	1728

TABLE 32

Comparison of Effort ( $M=1.35$ ,  $k=0.101$ , KFM, 6 Models)

	CPU Time (sec)	Storage I/O (K-min)	Disk I/O (EXCP)
Model 1	38.14	655.6	1717
Model 2	41.16	711.8	1812
Model 4	38.21	656.1	1717
Model 14	46.26	829.8	2052
Model 19	38.91	662.4	1716
Model 20	39.07	663.9	1716

TABLE 33

Pressure Distributions at Section 2 (Real,  $M=0.8$ ,  $k=0.153$ )  
for Various Models

Chord (%)	Model 1		Model 2		Model 19		Model 22 DLM	Dusto	Exp
	DLM	KFM	DLM	KFM	DLM	KFM			
3	8.10	7.28	8.06	7.24	8.06	7.38	8.04	17.40	-0.21
10	3.90	4.35	3.87	4.33	3.87	4.43	3.86	4.55	3.95
20	2.90	3.42	2.87	3.39	2.87	3.46	2.85	2.92	3.08
30	2.34	2.82	2.31	2.77	2.30	2.82	2.28	2.33	2.71
40	1.92	2.29	1.89	2.23	1.88	2.25	1.86	1.95	2.07
50	1.57	1.79	1.54	1.72	1.53	1.73	1.51	1.59	1.66
60	1.24	1.32	1.21	1.26	1.21	1.25	1.19	1.24	1.20
70	0.94	0.90	0.92	0.85	0.91	0.83	0.89	0.93	0.82
80	0.67	0.53	0.64	0.50	0.64	0.48	0.62	0.63	0.49
90	0.41	0.24	0.39	0.22	0.39	0.21	0.38	0.35	0.17
99	0.22	0.07	0.21	0.07	0.21	0.06	0.20	0.11	-

TABLE 34

Pressure Distributions at Section 2 (Imag,  $M=0.8$ ,  $k=0.153$ )  
for Various Models

Chord (%)	Model 1		Model 2		Model 19		Model 22 DLM	Dusto	Exp
	DLM	KFM	DLM	KFM	DLM	KFM			
3	-1.61	-2.43	-1.57	-2.38	-1.57	-2.26	-1.54	-6.55	0.32
10	-0.38	-1.25	-0.35	-1.21	-0.35	-1.11	-0.34	-1.12	-0.38
20	0.15	-0.46	0.16	-0.43	0.16	-0.30	0.18	-0.09	-0.04
30	0.48	0.21	0.49	0.23	0.49	0.39	0.50	0.40	0.34
40	0.71	0.74	0.72	0.76	0.71	0.93	0.72	1.44	0.64
50	0.86	1.10	0.87	1.11	0.86	1.27	0.87	0.92	0.59
60	0.94	1.26	0.95	1.26	0.95	1.41	0.95	1.07	0.69
70	0.95	1.21	0.95	1.21	0.95	1.32	0.96	1.10	0.57
80	0.88	0.97	0.88	0.96	0.88	1.04	0.88	1.01	0.55
90	0.69	0.58	0.69	0.57	0.69	0.60	0.69	0.76	0.34
99	0.45	0.03	0.45	0.03	0.47	0.03	0.45	0.32	-

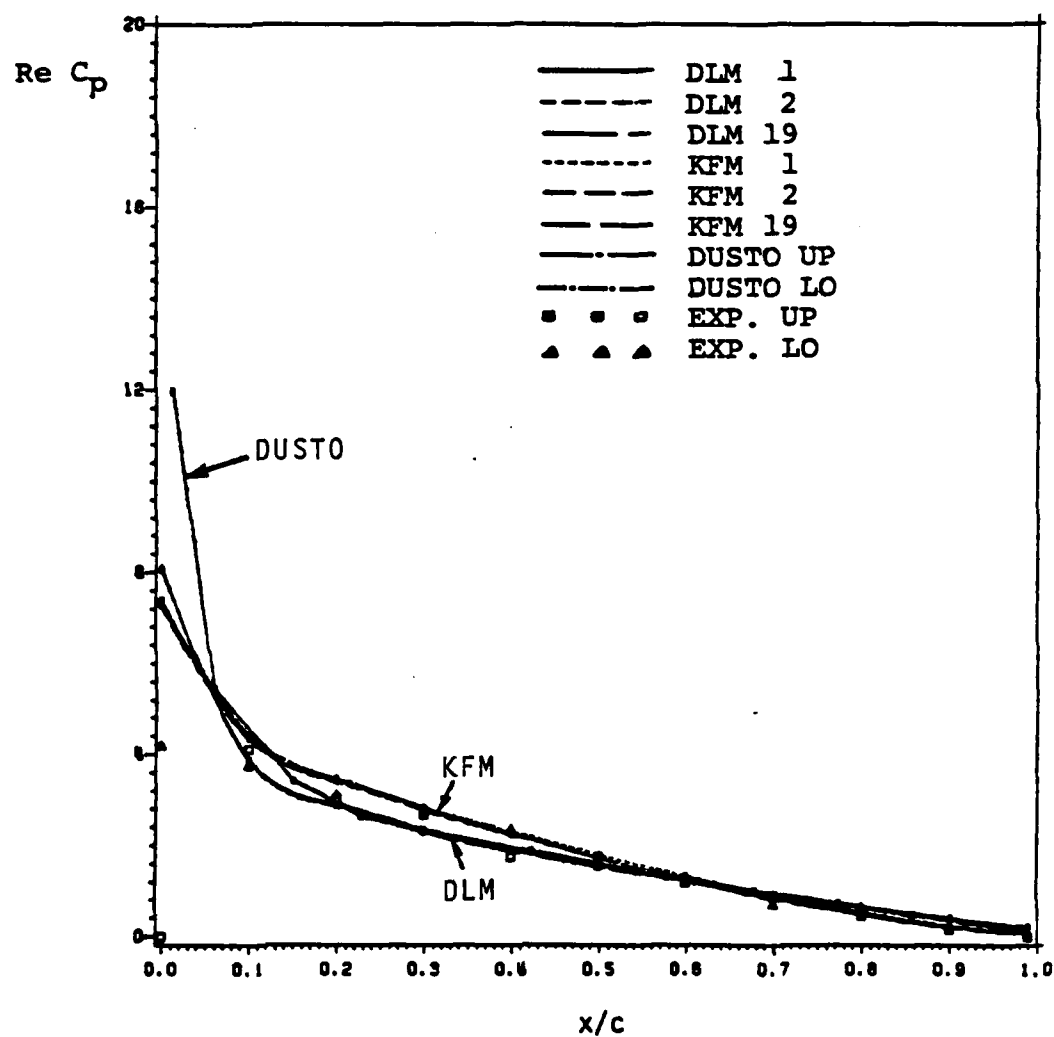


Figure 28: Pressure Distributions at Section 2 (Real,  $M=0.9$ ,  $k=0.153$ ) for Various Models

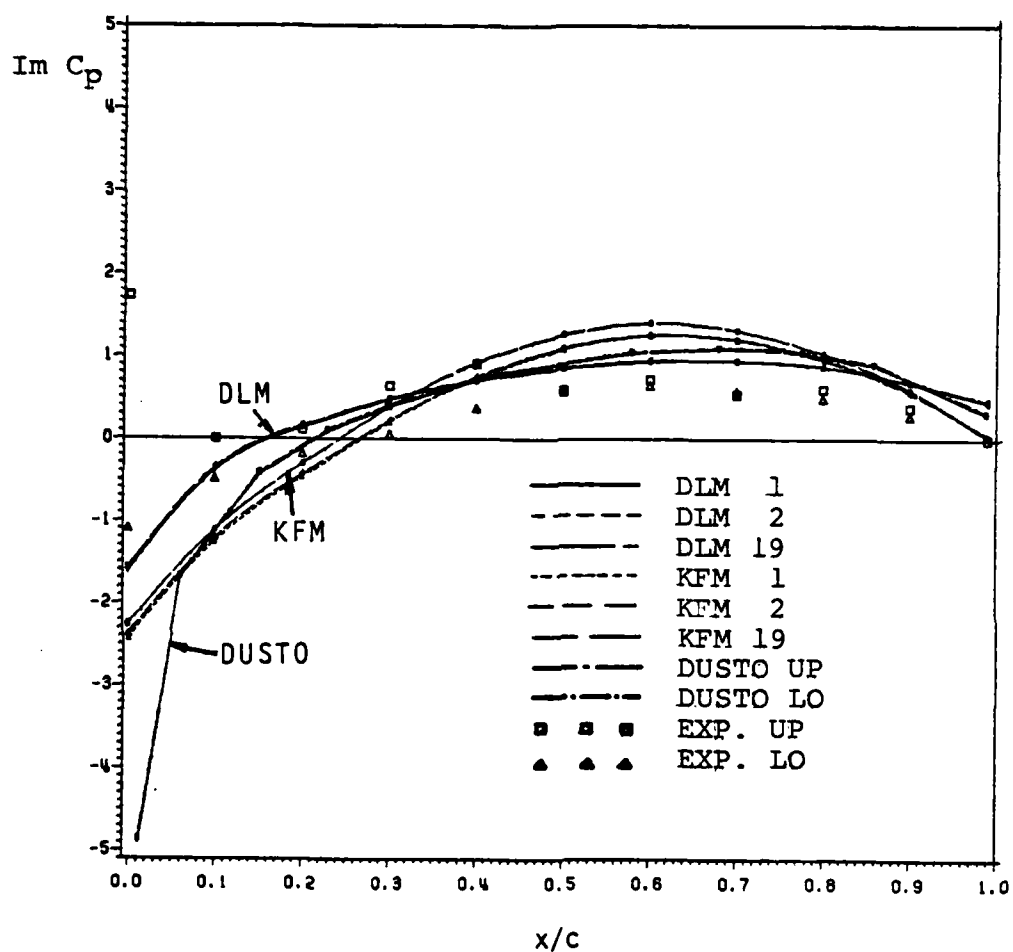


Figure 29: Pressure Distributions at Section 2 (Imag,  $M=0.8$ ,  $k=0.153$ ) for Various Models

TABLE 35

Pressure Distributions at Section 5 (Real,  $M=0.8$ ,  $k=0.153$ )  
for Various Models

Chord (%)	Model 1		Model 2		Model19		Model122	Dusto	Exp
	DLM	KFM	DLM	KFM	DLM	KFM	DLM		
3	11.84	10.59	11.70	10.43	11.68	10.67	11.62	24.32	0.66
10	5.47	5.54	5.38	5.40	5.37	5.50	5.32	6.04	4.75
20	3.83	3.93	3.75	3.78	3.73	3.82	3.67	3.54	3.98
30	2.88	3.04	2.80	2.90	2.80	2.90	2.73	2.59	3.27
40	2.21	2.37	2.14	2.24	2.13	2.23	2.06	2.03	2.28
50	1.69	1.82	1.63	1.71	1.62	1.68	1.56	1.56	1.74
60	1.27	1.35	1.22	1.25	1.22	1.22	1.16	1.14	1.20
70	0.94	0.94	0.89	0.87	0.90	0.84	0.85	0.82	0.75
80	0.66	0.59	0.62	0.54	0.63	0.52	0.59	0.56	0.44
90	0.41	0.31	0.38	0.28	0.39	0.27	0.36	0.33	0.14
99	0.22	0.14	0.21	0.01	0.21	0.01	0.20	0.11	-

TABLE 36

Pressure Distributions at Section 5 (Imag,  $M=0.8$ ,  $k=0.153$ )  
for Various Models

Chord (%)	Model 1		Model 2		Model19		Model122	Dusto	Exp
	DLM	KFM	DLM	KFM	DLM	KFM	DLM		
3	-1.73	-2.69	-1.65	-2.58	-1.65	-1.96	-1.59	-6.63	-0.18
10	-0.35	-1.03	-0.31	-0.97	-0.31	-0.46	-0.28	-1.12	-0.88
20	0.18	-0.28	0.21	-0.25	0.20	0.22	0.23	-0.09	-0.17
30	0.50	0.20	0.51	0.21	0.51	0.62	0.52	0.36	0.07
40	0.70	0.53	0.70	0.54	0.70	0.88	0.71	1.24	0.30
50	0.82	0.75	0.82	0.74	0.81	1.01	0.82	0.76	0.61
60	0.86	0.85	0.86	0.84	0.85	1.04	0.86	0.85	0.64
70	0.85	0.84	0.84	0.83	0.84	0.97	0.84	0.85	0.54
80	0.77	0.72	0.76	0.71	0.76	0.80	0.75	0.77	0.37
90	0.60	0.49	0.59	0.49	0.59	0.54	0.58	0.57	0.18
99	0.38	0.03	0.38	0.03	0.38	0.03	0.37	0.24	-

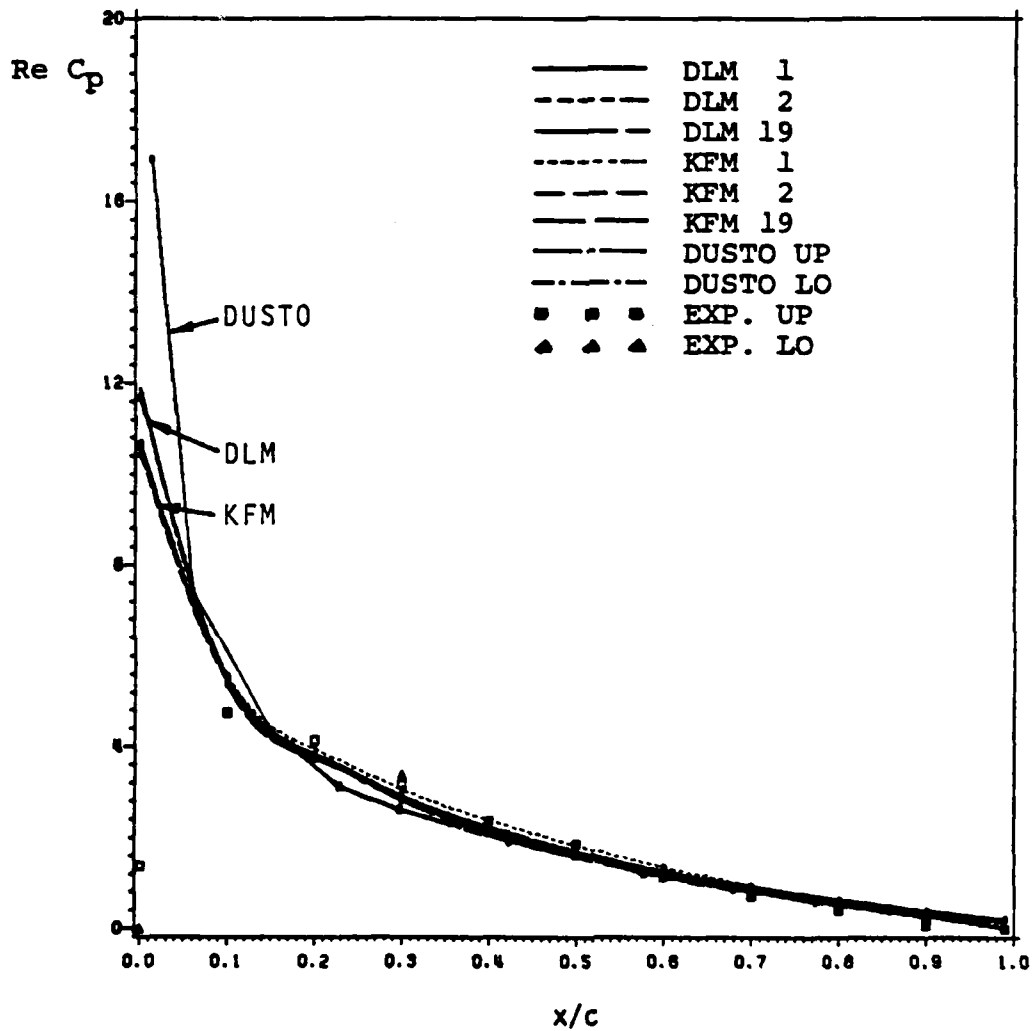


Figure 30: Pressure Distributions at Section 5 (Real,  $M=0.8$ ,  $k=0.153$ ) for Various Models

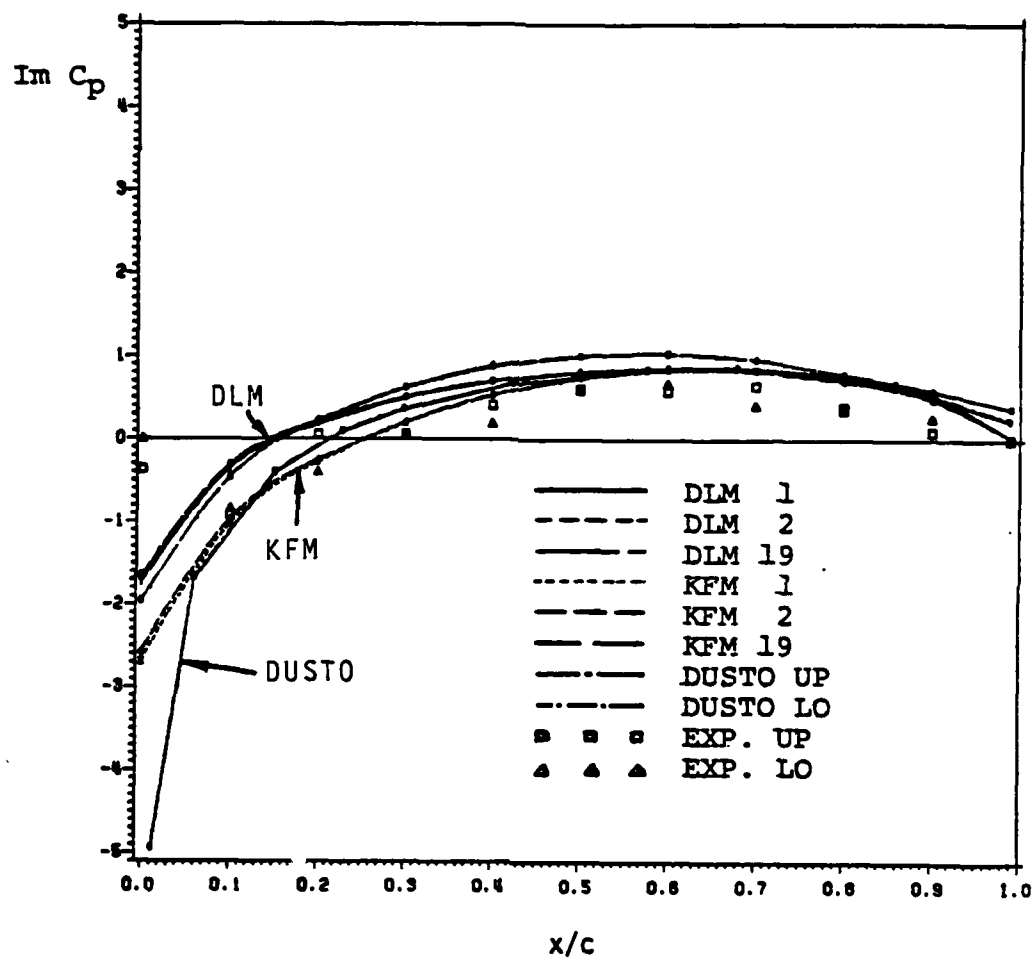


Figure 31: Pressure Distributions at Section 5 ( $Imag$ ,  $\eta=0.8$ ,  $k=0.153$ ) for Various Models



TABLE 37

Pressure Distributions at Section 8 (Real,  $M=0.8$ ,  $k=0.153$ )  
for Various Models

Chord (%)	Model 1		Model 2		Model19		Model122	Dusto	Exp
	DLM	KFM	DLM	KFM	DLM	KFM	DLM		
3	17.90	18.67	16.78	16.77	16.47	16.50	15.45	35.63	3.96
10	6.10	6.48	5.74	5.70	5.69	5.53	5.17	7.72	5.02
20	3.12	2.79	2.93	2.37	2.94	2.23	2.56	2.69	2.57
30	1.97	1.44	1.83	1.18	1.85	1.08	1.57	1.63	1.94
40	1.38	0.89	1.26	0.72	1.29	0.66	1.08	1.24	1.14
50	1.01	0.67	0.92	0.56	0.94	0.53	0.78	0.91	0.88
60	0.76	0.57	0.69	0.50	0.71	0.49	0.58	0.63	0.80
70	0.57	0.47	0.51	0.43	0.53	0.44	0.44	0.47	1.08
80	0.42	0.34	0.37	0.32	0.39	0.34	0.32	0.35	1.03
90	0.28	0.16	0.25	0.15	0.25	0.18	0.21	0.22	0.85
99	0.17	0.00	0.15	0.00	0.15	0.00	0.13	0.09	-

TABLE 38

Pressure Distributions at Section 8 (Imag,  $M=0.8$ ,  $k=0.153$ )  
for Various Models

Chord (%)	Model 1		Model 2		Model19		Model122	Dusto	Exp
	DLM	KFM	DLM	KFM	DLM	KFM	DLM		
3	-1.57	-2.51	-1.38	-2.37	-1.45	5.89	-1.22	-6.61	-0.58
10	-0.13	-0.51	-0.09	-0.52	-0.12	2.10	-0.06	-0.95	-0.93
20	0.32	0.07	0.32	0.02	0.30	0.94	0.31	0.17	0.08
30	0.49	0.24	0.48	0.19	0.46	0.53	0.45	0.43	0.37
40	0.57	0.30	0.55	0.26	0.53	0.40	0.50	1.05	0.35
50	0.61	0.35	0.58	0.32	0.56	0.41	0.53	0.57	0.36
60	0.61	0.41	0.58	0.39	0.56	0.49	0.52	0.59	0.47
70	0.58	0.49	0.55	0.49	0.54	0.58	0.50	0.57	0.36
80	0.53	0.57	0.50	0.57	0.49	0.63	0.45	0.51	0.44
90	0.42	0.58	0.40	0.57	0.39	0.58	0.37	0.39	0.11
99	0.30	0.06	0.28	0.06	0.27	0.05	0.25	0.19	-

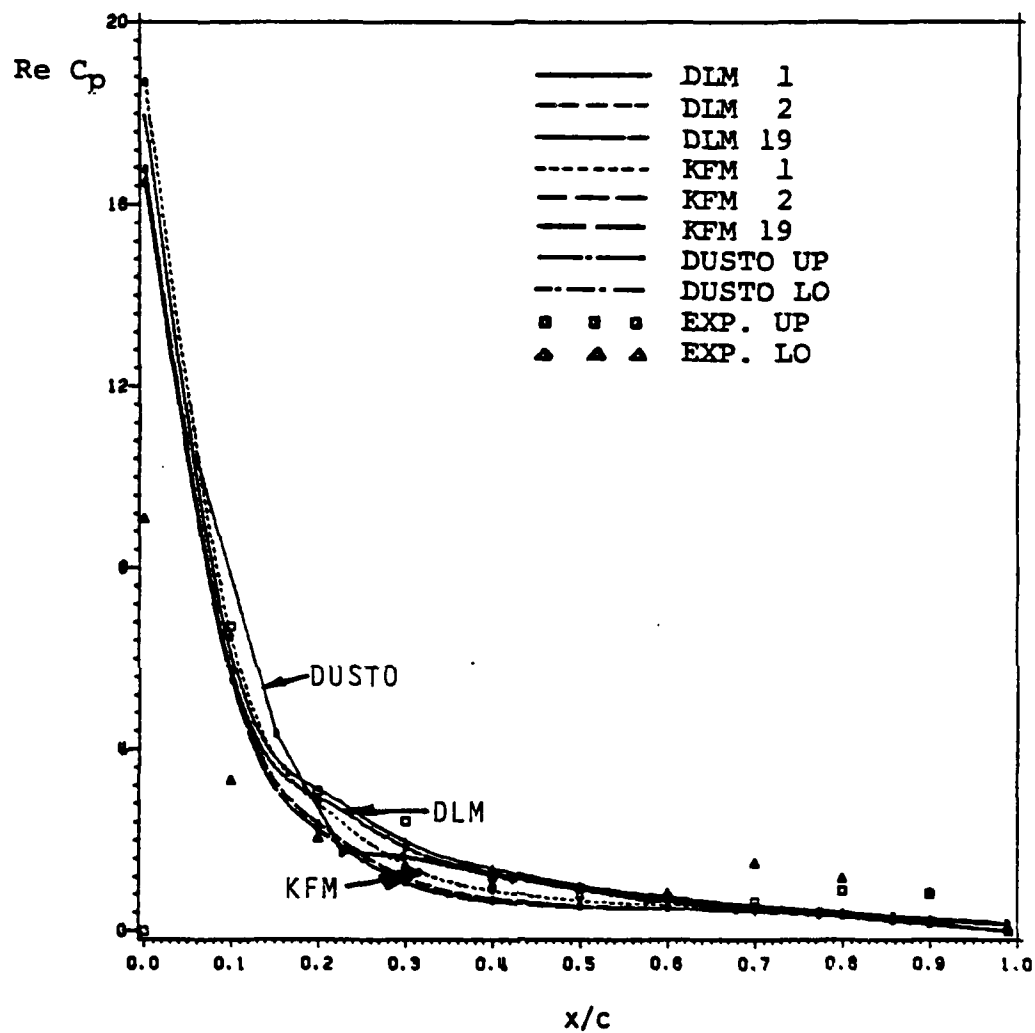


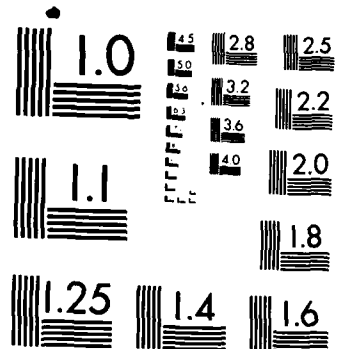
Figure 32: Pressure Distributions at Section 8 (Real,  $M=0.8$ ,  $k=0.153$ ) for Various Models

AD-A162 119 OPTIMIZATION OF TIP STORE MODELING(U) OKLAHOMA UNIV  
NORMAN SCHOOL OF AEROSPACE MECHANICAL AND NUCLEAR  
ENGINEERING A G STRIZ ET AL MAR 85 AFOSR-TR-85-1089  
UNCLASSIFIED AFOSR-83-0184 F/G 20/4

2/2

NL





MICROCOPY RESOLUTION TEST CHART  
NATIONAL BUREAU OF STANDARDS-1963-A

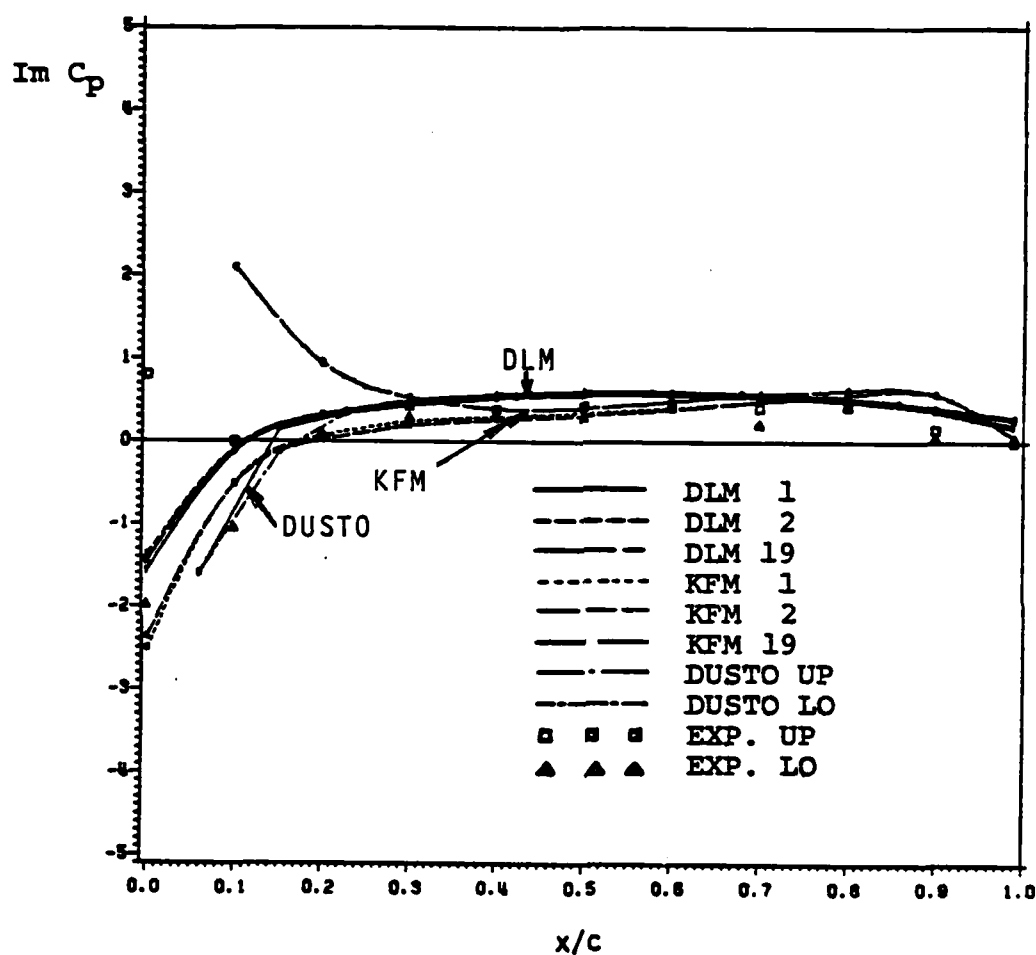


Figure 33: Pressure Distributions at Section 8 (Imag,  $M=0.8$ ,  $k=0.153$ ) for Various Models

In the DLM, since the pressures are calculated as the average values of the upper and lower surface pressures, the distribution of pressure should be inbetween the two experimental results. In the KFM, the pressure distributions are those of the upper surface, so the results of the KFM are expected to follow the shape of the upper surface results of the experimental data. As can be seen in the figures, both KFM and DLM show good agreement with the results of Dusto, and also show fairly good agreement with experimental results.

At section 2, the results of the KFM show better agreement than those of the DLM with the experimental results except at 10% - 20% chord. At section 8, both methods do not predict a small pressure rise near the trailing edge. For all cases, the real parts of the pressure show better comparison than the imaginary parts.

As can be seen in the figures, the flat plate model and the endplate models have very similar pressure distributions except at the tip-section. In general, the KFM displays somewhat more accurate distributions than the DLM.

## Chapter V

### CONCLUSION AND FUTURE WORK

#### 5.1 CONCLUSION

Calculations of the aerodynamic characteristics of an F-5 wing with and without a wing tip missile were carried out by two computer codes, a doublet lattice code (H7WC) and a kernel function code (ANKF). The unsteady lift distributions in spanwise direction and the unsteady pressure distributions in chordwise direction were computed for the wing with tip mounted launcher and missile without fins.

The following conclusions can be drawn from the performed analyses:

1. In almost all cases, the tip store can most economically and most accurately be represented by an endplate or a cylindrical slender body.
2. The tip store increases the load on the wing by a considerable amount especially in the tip region.
3. As the free stream velocity increases, the load is increased over the entire wing, but is decreased when the flow becomes supersonic.
4. The lift increases consistently with the complexity

of the store model. Also, complex models require more computer time and storage.

5. The kernel function method is very efficient with respect to computer cost. It seems to be nearly 3 times faster than the doublet lattice method and requires only about 1/3 of the effort of the doublet lattice method for all models. However, the doublet lattice method seems to yield slightly better results.
6. The endplate model 2 gives the best results for supersonic flow, while the endplate model 19 and the slender body model 22 seem to be better for subsonic flow.
7. All endplate models (2, 19, and 20) seem to be better than the present flat plate model for computing lift distributions of wings with tip stores.
8. Finally, the two methods show fairly good agreement with experimental results.

## 5.2 FUTURE WORK

In this paper, transonic flow was not treated as such. It was regarded as either a subsonic or supersonic flow. Therefore, further research is needed to account for transonic flow effects such as the shock wave. Secondly, the results from supersonic flow were not compared to experiment. In the future, a comparison is required to



ensure the validity of the results for the endplate models. Thirdly, it was assumed that the Mach number distribution be uniform over the entire wing. It is believed that this assumption caused errors in lift and pressure distributions, especially in the region from  $M=0.8$  to  $M=1.1$  where we can expect some shock wave near the trailing edge. However, this assumption was considered useful and necessary for the process of flutter computation when there are no experimental data for specific local Mach numbers over the wing available.

Also, the differences in pressure distributions on the upper and lower surfaces were neglected. Since the wing is not symmetric about the camber line, the aerodynamic characteristics of the upper surface and lower surface of the wing cannot be the same. More sophisticated codes are required to account for these differences.

Finally, the aspect most important for flutter analysis is the dynamic effect of the tip stores on the characteristics of the entire wing. Thus, further research is required in the way of performing flutter analysis by use of large aeroelastic codes such as FASTOP or MSC/NASTRAN. These analyses should compare the flutter results of the presently used flat plate models to those obtained with the aerodynamics for the endplate and maybe slender body models for both KFM and DLM. Additionally, flight test results or wind tunnel test results should be used for comparison and

evaluation. If the new models should prove advantageous, similar analyses to the one presented here could be performed for other tip stores and even underwing stores.

## REFERENCES

1. Chadwick, W.R., "External-Store Loads Using Nonplanar Lifting Surface Theory", Journal of Aircraft, Vol. 11, March 1974, pp. 181-188.
2. Kraus, W., Panel Methods in Aerodynamics: Numerical Methods in Fluid Dynamics, Hemisphere Publishing Co. 1978, pp. 237-297.
3. Martin, F.W., Saunders, G.H., and Smith, C.J., "Image System Solution for Store Aerodynamics with Interference", Journal of Aircraft, Vol. 12, March 1975, pp. 151-155.
4. Roos, R., Bennekens, B., and Zwaan, R.J., "Calculation of Unsteady Subsonic Flow about Harmonically Oscillating Wing/Body Configurations", Journal of Aircraft, Vol. 14, May 1977, pp. 447-454.
5. Parker, D.L., "Doublet Lattice Aerodynamic Predictions for an Oscillating F-5 Wing with Stores", AFIT/GAE/AA/77-D-10, Air Force Institute of Technology, Dec. 1977.
6. Cenko, A., Tinoco, E.N., Dyer, R.D., and DeJongh, J., "PAN AIR Applications to Weapons Carriage and Separation", Journal of Aircraft, Vol. 18, Feb. 1981, pp. 128-134.
7. Dusto, A.R., "Aerodynamic Analysis of a Fighter Aircraft with a Higher Order Paneling Method", AFWAL-TR-80-3115, Air Force Wright Aeronautical Laboratories, Nov. 1980.
8. Sotomayer, W.A., Dusto, A.R., Epton, M.A., and Johnson, F.T., "Aerodynamic Modeling of an Oscillating Wing with External Stores", AIAA Paper 81-0648, Atlanta, Ga., April 1981.
9. Tijdeman, H., van Nunen, J.W.G., Kraan, A.N., Persoon, A.J., and Poestkoke, R., "Transonic Wind Tunnel Tests on an Oscillating Wing with External Stores. Parts I-IV", AFFDL-TR-78-194. Parts I to IV, Air Force Flight Dynamics Lab., 1978-1979.

10. Noll, T.E., Huttzell, L.J., and Cooley, D.E., "Wing/Store Flutter Suppression Investigation", Journal of Aircraft, Vol. 18, Nov. 1981, pp. 969-975.
11. Wilkinson, K., et al., "An Automated Procedure for Flutter and Strength Analysis and Optimization of Aerospace Vehicles", AFFDL-TR-75-137, Vols. I and II, Air Force Flight Dynamics Lab., Dec. 1975.
12. Pollock, S.J., Sotomayer, W.A., Huttzell, L.J., and Cooley, D.E., "Evaluation of Methods for Prediction and Prevention of Wing/Store Flutter", Journal of Aircraft, Vol. 19, June 1982, pp. 492-498.
13. Woodward, F.A., "Analysis and Design of Wing-Body Combinations at Subsonic and Supersonic Speeds", Journal of Aircraft, Vol. 5, No. 6, Nov.-Dec. 1968, pp. 528-534.
14. Ferman, M.A., and Unger, W.H., "A New Approach for Rapid Flutter Clearance of Aircraft with External Stores", Proceedings of the Aircraft/Stores Compatibility Symposium, Sacramento, Ca., Sept. 1973, pp. 113-137.
15. Triplett, W.E., "Wind Tunnel Correlation Study of Aerodynamic Modeling for F/A-18 Wing-Store Tip-Missile Flutter", Journal of Aircraft, Vol. 21, May 1984, pp. 329-334.
16. Turner, C.D., "Effect of Store Aerodynamic on Wing/Store Flutter", Journal of Aircraft, Vol. 19, July 1982, pp. 574-579.
17. Chapman, D.R., "Computational Aerodynamics Development and Outlook", AIAA Journal, Vol. 17, Dec. 1979, pp. 1293-1313.
18. Cunningham, A.M. Jr., "A Steady and Oscillatory Kernel Function Method for Interfering Surfaces in Subsonic, Transonic, and Supersonic Flow", NASA CR-144895, Sept. 1976.
19. Giesing, J.P., Kalman, T.P., and Rodden, W.P., "Subsonic Unsteady Aerodynamics for General Configurations", Part I, Vol. I-II, AFFDL-TR-71-5, Nov. 1971.
20. Giesing, J.P., Kalman, T.P., and Rodden, W.P., "Subsonic Steady and Oscillatory Aerodynamics for Multiple Interfering Wings and Bodies", Journal of Aircraft, Vol. 9, Oct. 1972, pp. 693-702.

21. James, R.M., "On the Remarkable Accuracy of the Vortex Lattice Discretization in Thin Wing Theory," Report DAC-67211, Feb. 1969, McDonnell Douglas Corp., Long Beach, California.

**END**

**FILMED**

---

**1-86**

**DTIC**